An enhanced semi-analytical estimation of tool-chip interface temperature in metal cutting

Journal of Manufacturing Processes 105 (2023) 407–430

Contents lists available at ScienceDirect

Journal of Manufacturing Processes

journal homepage: www.elsevier.com/locate/manpro

An enhanced semi-analytical estimation of tool-chip interface temperature in metal cutting

Charlie Salame, Amir Malakizadi *

Department of Industrial and Materials Science, Chalmers University of Technology, SE-412 96 Gothenburg, Sweden

ARTICLE INFO

Keywords:
Temperature
Simulation
Cutting
Crater wear
Carbon steels

ABSTRACT

An accurate estimation of the temperature distribution on tool surfaces is of great industrial importance; without it, a reliable prediction of tool wear in machining, especially thermally-induced wear mechanisms such as dissolution-diffusion and oxidation, is deemed impossible. This has promoted the development of semi-analytical models for simulation of the tool-chip interface temperature, which are less time-intensive and reasonably accurate.

This study aims to present an enhanced prediction of the tool-chip interface temperature within the context of the available semi-analytical solutions of the heat conduction-advection problem with a moving heat source. A novel approach is presented to obtain the variable heat flux along the tool-chip interface based on a non-uniform contribution of generated heat in the sticking and sliding zones during chip flow. The capability of the enhanced model to simulate the temperature distribution is demonstrated for machining C45 and C50 plain carbon steels using uncoated carbide tools. The predictions are validated against the results of experimental orthogonal cutting tests for the same cutting conditions. A comparative analysis is then performed to underline the importance of incorporating the variable heat flux for reliable predictions of the maximum interface temperature and its location on the rake face. The outlook for future developments is also highlighted.

1. Introduction

The demands for higher productivity and better quality, along with the tighter protocols for sustainable machining, have obliged the associated manufacturing sectors to become increasingly vigilant about implementing the optimised range of cutting conditions, timely tool-change scheduling, and minimum overall scrap rates. A robust and sustainable machining operation necessitates consistency in tool life prediction during the process to avoid loss of dimensional tolerances and poor surface quality owing to the worn tool geometry [1].

The tool wear in machining develops through an intricate synergy of different mechanisms such as abrasion, adhesion, plastic deformation, and dissolution-diffusion [2]. Factors such as the cutting conditions and material properties of the tool and workpiece all influence the intensity with which a certain wear mechanism contributes to the overall wear evolution on the cutting edge. In particular, the progression of thermally-induced wear types, namely crater wear and plastic deformation, are highly dependent on the temperature distribution across the tool-chip-workpiece interfaces [1]. The currently available experimental techniques for measuring tool temperature are often fallible, given the limited accessibility of the cutting zone and the intricate dimensions in metal cutting [3]. This is only worsened by the narrow shear zones, chip obstacles and complex contact phenomena on the rake face, where both tool and chip are in continuous motion relative to each other [4].

The available techniques for temperature measurement during metal cutting can be generally classified into three categories: direct conduction, indirect radiation and metallographic [4]. While traditional measurement instruments such as tool-workpiece thermocouples can be used for direct conduction measurements, they often only allow the measurement of average temperatures [5]. More advanced technologies such as charge-coupled device sensors and electronics have been developed to obtain temperature profiles of the tool-chip geometry by infrared detection. However, such technologies have shown only limited application in practice owing to calibration and sensitivity issues and limited view fields. These limitations have restricted them mostly to measuring temperature in dry machining. Experimental techniques for temperature measurement in cutting processes and their limitations have been discussed thoroughly by Komanduri and Hou [6], O'Sullivan and Cotterell [7], and more recently Liu et al. [8]. These experimental difficulties present the need for thermal modelling of the cutting process, not only to improve the predictability and understanding of underlying

* Corresponding author.
E-mail address: amir.malakizadi@chalmers.se (A. Malakizadi).

https://doi.org/10.1016/j.jmapro.2023.09.015
Received 28 June 2023; Received in revised form 31 August 2023; Accepted 5 September 2023
Available online 29 September 2023

Nomenclature

A_a, $A_a^{'}$	Geometric factors for the calculation of the heat partition (−)
B_{chip}	Heat partition going into the chip (−)
B_{tool}	Heat partition going into the tool (−)
c	Specific heat of workpiece material (J/kg°C)
f	Feed rate (mm/rev)
F_f	Friction force (N)
F_n	Normal force (N)
F_s	Shear force acting on the shear plane (N)
F_c	Cutting force (N)
F_t	Feed force (N)
F_N	Projected component of the normal force in the cutting direction (N)
F_T	Projected component of the shear force in the cutting direction (N)
$F_N^{'}$	Projected component of the normal force in the feed direction (N)
$F_T^{'}$	Projected component of the shear force in the feed direction (N)
h_a	Uncut chip thickness for a rounded cutting edge (mm)
h_p	Ploughing depth (mm)
h_u	Uncut chip thickness for an ideal cutting edge (mm)
k_t	Thermal conductivity of the tool (W/m.K)
k_w	Thermal conductivity of the workpiece material (W/m.K)
KM	Location of maximum crater wear depth on the contact length (mm)
k_{SSZ}	Shear strength of the workpiece material in the SSZ (MPa)
l_{st}	Length of sticking zone (mm)
l_{tr}	Length of transition zone (mm)
l_{sl}	Length of sliding zone (mm)
l_p	Ploughing length on the flank face of the tool (mm)
l_{sh}	Length of shear plane (mm)
l_c	Contact length between the chip and the tool's rake face (mm)
l_i	Position of the differential segment of the band heat source (mm)
n	Exponential constant for the shear stress distribution (−)
N	Number of the discrete points at the tool-chip interface (−)
q	Heat flux applied to a given boundary (J/mm^{2}s)
q_{PSZ}	Heat flux in the primary shear zone (J/mm^{2}s)
q_{SSZ}	Heat flux in the secondary shear zone (J/mm^{2}s)
$q_{SSZ,max}$	Maximum heat flux in the secondary shear zone for a variable heat flux (J/mm^{2}s)
q_{pli}	Heat flux of the induced plane heat source in the primary shear zone (J/mm^{2}s)
r_c	Chip thickness ratio (−)
r_e	Edge radius of the tool (μm)
R_1, $R_1^{'}$	Distance between the primary shear heat source and the point of interest M in the chip (mm)
R_2, $R_2^{'}$	Distance between the secondary shear heat source and the point of interest M in the chip (mm)
R_3, $R_3^{'}$	Distance between the secondary shear heat source and the point of interest M in the tool (mm)
t_c	Cut chip thickness (mm)
T_0	Initial temperature applied to a given boundary (°C)
T_{max}	Maximum temperature obtained experimentally (°C)
$\Delta T_{chip,PSZ}$	Temperature rise in the chip due to the heat from the primary shear zone (°C)
$\Delta T_{chip,SSZ}$	Temperature rise in the chip due to the heat from the secondary shear zone (°C)
$\Delta T_{tool,PSZ}$	Temperature rise in the tool due to the heat from the primary shear zone (°C)
$\Delta T_{tool,SSZ}$	Temperature rise in the tool due to the heat from the secondary shear zone (°C)
$T_{chip,i}$	Temperature at each discrete point i along the tool-chip interface on the chip side (°C)
$T_{tool,i}$	Temperature at each discrete point i along the tool-chip interface on the tool side (°C)
$\bar{T}_{PSZ}$	Average temperature at the primary shear plane (°C)
$T_{C,max}$	Maximum temperature calculated at the interface on the chip side (°C)
$T_{T,max}$	Maximum temperature calculated at the interface on the tool side (°C)
V_{sh}	Shear velocity (mm/s)
V_{ch}	Chip velocity (mm/s)
V_c	Cutting speed (m/min)
$V_{\chi,\psi}$	Chip velocity at the tool-chip interface (mm/s)
w	Width of cut (mm)
X_j	j^{th} vector containing the Komanduri and Hou functional parameters
α	Clearance angle (°)
α_w	Thermal diffusivity of the workpiece material (mm^2/s)
α_t	Thermal diffusivity of the tool (mm^2/s)
γ	Rake angle (°)
γ_s	Shear strain (−)
$\dot{\gamma}$	Shear strain rate (1/s)
δ	Maximum thickness of secondary shear zone (mm)
η	Taylor-Quinney coefficient (−)
θ_s	Stagnation angle (°)
κ, χ, ψ	Non-dimensional local coordinates (−)
ξ	Exponential constant of normal stress distribution (−)
λ	Friction angle (°)
ρ	Density of workpiece material (kg/m^2)
σ	Normal stress acting on the tool's rake face (MPa)
σ_0	Maximum normal stress acting on the tool's rake face (MPa)
τ	Shear stress acting on the tool's rake face (MPa)
ϕ	Shear angle (°)
Ω, ϱ, ς	Constants to ensure continuity between sticking and sliding zones (−)
ΔB, m, k, C, $\Delta\widetilde{B}$, $\widetilde{m}$, $\widetilde{k}$, $\widetilde{C}$	Model parameters associated with the calculation of the variable heat partitioning in Model I (−)

tool wear mechanisms from a scientific perspective, but also to push the limits of high-performance machining from an industrial point of view. Specifically for industrial applications, it is important that a model is capable of accurately predicting the cutting forces, stresses, temperature fields and ultimately the tool wear, given that the cutting conditions and thermo-mechanical properties of the workpiece and tool are known.

Current literature includes a plethora of modelling methods for prediction of temperature distribution in machining. These methods can predominantly be classified as numerical, analytical or semi-analytical approaches and may be compared with respect to accuracy, adaptability and computational efficiency. While the numerical methods give higher flexibility regarding the cutting geometries, boundary conditions and thermo-mechanical coupling, their industrial application is rather limited for being computationally more intensive [9,10]. The methods that rely on the chip formation simulation for estimation of tool-chip-workpiece interface temperature require a large pool of thermo-mechanical data to be predetermined through extensive experimental efforts for given workpiece and tool material combinations [4]. These

are in addition to the frictional properties and separation/damage criteria that are generally needed for the chip formation simulations. To evade these challenges and limitations, researchers have proposed several analytical solutions to the heat conduction problem with a moving heat source. These methods, though very efficient, may be less accurate because of the oversimplified underlying assumptions [11]. Here, a distinction may be drawn between analytical and semi-analytical models based on the methods used for derivation of their model inputs and boundary conditions. While most analytical models rely on boundary conditions (e.g., heat flux) that are obtained using the classic metal cutting theories, semi-analytical models may additionally benefit from numerical methods to determine the required boundary conditions. The semi-analytical methods combine the agility of analytical methods with the superior adaptability of numerical methods, allowing for more accurate estimations.

The early attempts to quantify and predict the thermal effects. In metal cutting date back to the late 1930s to mid-1940s, when Rosenthal [12], Jaeger [13] and Blok [14] presented innovative solutions for the heat conduction problem with the moving heat source [4]. For example, Blok's partition principle was based on calculating two values of the mean temperature at the tool-chip interface using two different approaches, then equating those temperature fields to obtain the heat partition value (flowing into the tool) as follows: one approach considered a stationary heat source at the rake face of the tool, and the other considered a moving heat source of constant flux moving at the speed of the chip at the separating surface of the chip [14]. His pioneering work on the analytical prediction of temperatures during machining was soon followed by major contributions from Hahn [15], Trigger and Chao [16], and Loewen and Shaw [17].

Trigger and Chao [16] and Loewen and Shaw [17] established analytical models that calculated the temperature along the tool-chip interface during orthogonal machining based on Blok's principle. The main criticism of these models was their use of Blok's partition principle, which assumes a uniform heat flux along the tool's rake face, an assumption that does not accurately represent the real cutting conditions. In addition, both models considered the workpiece material and chip as two separate bodies in relative sliding motion at the primary shear plane. This implied that the heat generation at the primary shear zone (PSZ) was partitioned between the workpiece and chip, leading to further assumptions regarding the ratio of that partition. However, as pointed out by Hahn [15] and later by Komanduri and Hou [18], the chip and work material cannot be modelled as two separate bodies, as the formation of the chip is a material flow process which is significantly different from sliding contact between separate bodies [18]. To account for the heat-carrying flow of material during cutting, Hahn [15] developed a totally novel approach to heat source calculations that did not require a priori knowledge of heat partition between the chip and workpiece. Hahn's model was based on an oblique band heat source moving inside the workpiece material obliquely at the speed of cutting. This was a more realistic assumption, since the workpiece material continuously undergoes plastic deformation at the shear plane and passes through it to form the chip. Three decades later, Wright et al. [19] presented another notable solution to the heat conduction problem with a moving heat source using the Laplace transform. The authors included the heat contributions from both the sticking and sliding zones, and therefore the factual tribological conditions at the tool-chip interface were taken into account. This model assumed a constant heat partition between the tool and chip and was only able to predict the interface temperature. In line with this approach, Moufki et al. [20] proposed an extended solution incorporating the temperature-dependent Coulomb friction law to account for sticking-sliding tribological conditions at the tool-chip interface using a single mathematical expression. In addition, their solution allowed for temperature estimation within the entire chip domain, in contrast to the original solution by Wright et al. [19]. Nevertheless, the extensive thermal model developed by Komanduri and Hou [18,21,22] is perhaps the most commonly used analytical model for temperature estimation in cutting. This model combines an extension of Hahn's oblique moving heat source model for the PSZ with Chao and Trigger's stationary rectangular heat source for the secondary shear zone (SSZ) as well as the heat source method developed by Jaeger. This model includes a variable heat partition along the tool-chip interface; however, it still assumes a constant and uniform heat source at the corresponding surfaces.

Several researchers, for example, Li et al. [23], Huang and Liang [24], M'Saoubi and Chandrasekaran [25], Karpat and Özel [26,27], Shan et al. [28], Akbar and Arsalan [29], and Zhou et al. [30], have proposed different modifications to incorporate variable heat flux to improve the predictability within the context of this model. Shan et al. developed a modification to the analytical models by Komanduri and Hou and Huang-Liang in order to incorporate the effect of the relief angle during orthogonal cutting of Ti-6Al-4V [28]. Avevor et al. [31] developed a hybrid analytical-numerical model based on the Petrov-Galerikin formulation, where the frictional heat source was applied using a Dirac function. In their recent model, Veiga et al. [32] converted the non-linear heat conduction problem into a linear one using the Kirchhoff transform in order to incorporate the temperature dependence of the thermal properties of the tool and workpiece material. Similarly, Weng et al. [33] proposed an enhancement to the model by Komanduri and Hou in order to include the temperature-dependent thermal properties of the tool and workpiece. Further research was conducted by Barzegar and Ozlu [34] as well as Hu et al. [35] in order to investigate the effect of additional heat sources at the tool tip for tools that are honed or chamfered, respectively. Liu et al. [36] developed a three-dimensional analytical model for transient tool temperature modelling that can also incorporate the convection effect due to cutting fluids.

Despite the vast number of studies, there seems to be a lack of consensus about multiple assumptions in the proposed analytical models for modelling and simulating tool temperature in metal cutting. While the models proposed by Wright et al. [19] and Moufki et al. [20] assume a constant heat partition along the tool-chip interface and a variable heat flux distribution, the model developed by Komanduri and Hou and its modifications adopt a non-uniform heat partition distribution between the tool and chip along the interface and instead includes a constant heat flux [18,21,22]. On the other hand, some of the proposed modifications of Komanduri and Hou's model do not fully comply with the well-documented tribological conditions at the tool-chip interface. For example, some studies fail to include the effects of these tribological conditions on the heat generation in the sticking zone through a physics-based quantification of the shear deformation on the tool surface [28,37]. Evidently, the variation of shear stresses, sliding velocity and rate of deformation within the sticking zone need to be included to improve the prediction results [38]. These have led to the inconsistencies in predicting results concerning the estimated maximum temperature or the temperature distribution on the rake face of the tool. A reliable estimation of temperature distribution on the tool's rake face is vital for an accurate prediction of crater wear geometry.

This study aims to extend the well-established analytical models proposed by Komanduri and Hou [18,21,22] and Moufki et al. [20], referred to as Models I and II respectively, to account for the effects of variable heat flux. This extension is postulated based on a physics-based understanding of tribological conditions at the tool-chip interface. While it is possible to include a variable heat partition between the tool and chip in Model I, the underlying assumptions of Model II only allow for incorporating a constant heat partition between the tool and chip. Hence, a variable heat partition was only incorporated into Model I. Table 1 summarises the various scenarios investigated in the current study. Apart from the variable heat flux and heat partitioning, the role of the cutting-edge radius and ploughing force in the intensity of generated heat is also studied using a detailed analysis of normal and shear stress distributions around the cutting edge [39,40]. A comparative analysis is then performed within the context of Models I and II to, for example, reveal the role of variable heat flux and its parameters, heat partition

Table 1
Various assumptions examined in this study within the context of Komanduri and Hou's [18,21,22] and Moufki et al.'s [20] analytical models.

Designation	Variable heat flux	Variable heat partition
Model I (C)[a]	×	✓
Model I (V)	✓	✓
Model II (C)[b]	×	×
Model II (V)	✓	×

[a] Model I: Komanduri and Hou [18,21,22].
[b] Model II: Moufki et al. [20].

equations, and ploughing force on the temperature distribution on the rake face.

This article is structured as follows. Section 2 presents the experimental data used to validate the model's predictions for orthogonal machining of C45 and C50 plain carbon steels using uncoated cemented carbide tools. The theoretical bases of the heat transfer in machining, including the presentation of the heat conduction problem, heat generation during chip formation and derivation of an expression for variable heat flux on the tool's rake face, are given in Section 3. The original framework of Komanduri and Hou's and Moufki et al.'s models and the implemented modifications are presented in Section 4. Section 5 summarises the simulation results in a comparative manner and highlights the potentials for further improvements.

2. Experimental data

The experimental data for C45 steel was taken from [41]. The authors performed dry orthogonal cutting tests on a CNC vertical milling machine. The cylindrical specimens were of diameter 58 ± 0.05 mm with a wall thickness (i.e., width of cut: w) of 2 ± 0.02 mm. Uncoated tungsten carbide inserts (TPUN 160308) with an edge radius of 40 μm were mounted on a CTGPR 2020K–16 tool holder, resulting in a clearance angle of 6° and a rake angle of 5°. The cutting and feed forces were measured using a dynamometer (Kistler 9121), while the temperature measurements of the cutting zone were performed using a FLIR Titanium 550 M infrared camera. Table 2 summarises the experimental measurements including the cutting and feed forces (F_c and F_t, respectively), tool-chip contact length (l_c), chip thickness (t_c) and maximum temperature on the rake face (T_{max}) obtained for each cutting condition. Machining tests were repeated at least 3 times to ensure the repeatability of measured data.

For C50 plain carbon steel, the orthogonal cutting tests were conducted on an EMCO TURN 365 CNC lathe equipped with a three-component dynamometer (Kistler 9257A). The uncoated carbide inserts (TCMW 16T304-H13A) were mounted on an STGCR 2020K-16 tool holder, resulting in a rake angle of 0° and a clearance angle of 7°. The edge radius of the inserts was within the 20 ± 2 μm range, and machining tests were performed for a spiral cutting length of 30 m. The experimental setup used for machining tests is shown in Fig. 1.

After the cuts were performed, the inserts were etched with a diluted HCl solution to remove the adhered material, i.e., built-up layer (BUL), to expose the tool's surfaces. The tools were then examined using a Sensofar S neox optical profilometer to obtain the crater wear dimensions. The maximum crater depth (*KT*) and its location (*KM*) were then determined according to ISO-3685 standard for validation of model predictions, as shown in Fig. 2. The inserts were further examined using scanning electron microscopy (SEM) with the Zeiss GeminiSEM 450. The imaging was acquired using backscattered electrons to identify the sticking zone at the tool's rake face, as well as qualitatively compare the surface topography between the sticking, sliding and unworn tool surface.

Table 3 summarises the experimental measurements, including the cutting and feed forces, tool-chip contact length, chip thickness and location of maximum crater wear depth on the rake face (*KM*) in five different cutting conditions.

Table 2
Experimental results obtained for orthogonal cutting of C45 steel [41]. $w = 2 \pm 0.02$ mm.

Condition	V_c (m/min)	f (mm/rev)	F_c (N)	F_t (N)	l_c (mm)	t_c (mm)	T_{max} (°C)
1	100	0.1	561 ± 10	424 ± 24	0.43 ± 0.07	0.320 ± 0.010	542 ± 41
2	100	0.2	938 ± 20	578 ± 30	0.82 ± 0.09	0.514 ± 0.006	665 ± 48
3	200	0.1	517 ± 7	370 ± 14	0.55 ± 0.03	0.246 ± 0.015	855 ± 84
4	200	0.2	854 ± 22	450 ± 16	0.77 ± 0.05	0.412 ± 0.014	1033 ± 85

3. Heat transfer in machining – theoretical foundations

The temperature distribution in the chip and tool can be obtained by solving the conduction problem. The semi-analytical models generally present a solution to the heat transfer problem with moving and/or stationary heat sources to account for heat generation in the shear zones and friction. Essentially, these models assume that the heat transfer during chip formation is analogous to the heat transferred by an inclined band source moving through a (semi-) infinite plane. These models further assume that the local temperature rise associated with the primary and secondary shear band sources can be superimposed to obtain the complete temperature distribution of the chip. The heat transfer in the chip sliding over the tool's rake surface with the velocity V_{ch} can be described using the following differential equation – referred to as the conduction-advection equation in 2D:

$$-\nabla(k(T)\nabla T) + \rho(T)c(T)V_{ch}(x,y)\nabla T = 0 \tag{1a}$$

Subject to the following boundary conditions:

$$-k(T)\nabla T = q \quad \text{on boundary } S_q \tag{1b}$$

$$T = T_0 \quad \text{on boundary } S_T \tag{1c}$$

where $k(T)$, $\rho(T)$ and $c(T)$ represent the temperature-dependent thermal conductivity, density and specific heat of the workpiece material, respectively. q and T_0 are the heat flux and temperature applied to the corresponding boundaries S_q and S_T, respectively. The heat transfer in the tool is only governed by the conduction, and thus the term associated with the heat transferred by the material transport in Eq. (1a) is eliminated for temperature prediction in the tool. Boothroyd [42] and later Komanduri and Hou [18] thoroughly reviewed the proposed solutions of Eq. (1a) based on the underlying assumptions concerning the moving heat source and boundary conditions. The key parameters with marked impacts on the temperature in the chip and tool are the heat flux imposed on the tool-chip interface and the heat partition coefficient determining the portion of the heat that is divided between the chip and tool, respectively [8]. These parameters will be discussed in detail in Section 4 to create a baseline for further modification of the analytical models of Komanduri and Hou [18,21,22] and Moufki et al. [20].

3.1. Heat generation during chip formation – ideal cutting-edge geometry

Heat generation in metal cutting depends on several factors, including the thermo-mechanical properties of the workpiece material, tribological conditions at the tool-chip interface, applied cutting conditions and cutting tool geometry. The majority of studies concerning the semi-analytical prediction of temperature in orthogonal cutting rely on the classical metal cutting models, e.g., that of Merchant [43], to determine the generated heat in the PSZ and SSZ. These theories most often assume an ideal cutting-edge geometry to simplify the complex

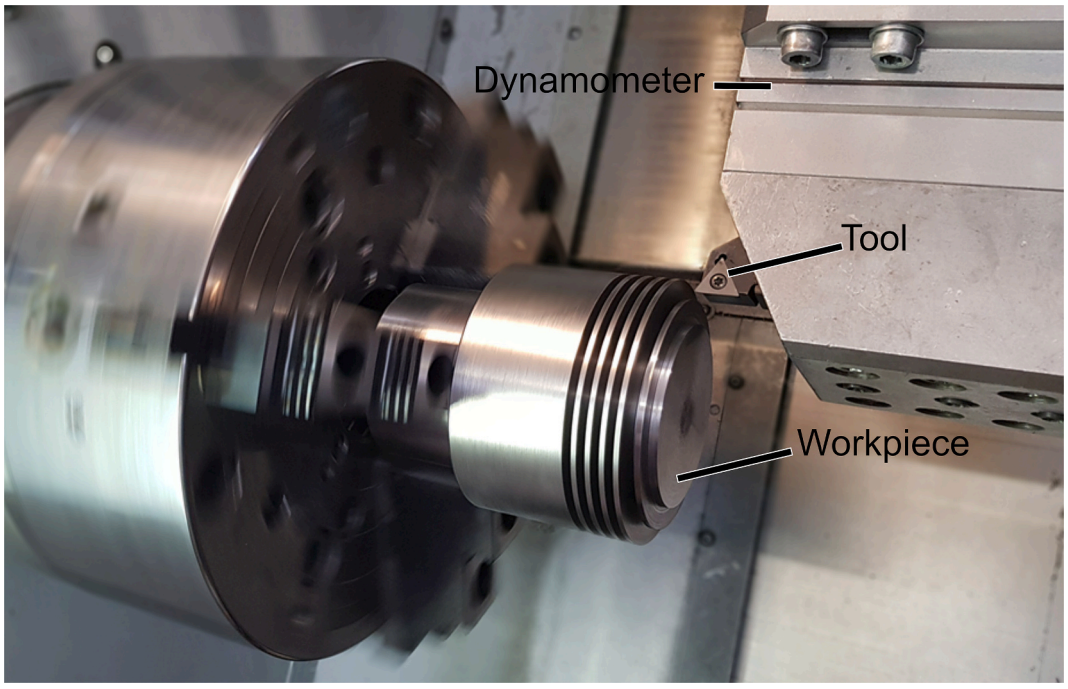

Fig. 1. Experimental setup used for dry orthogonal cutting of C50 steel.

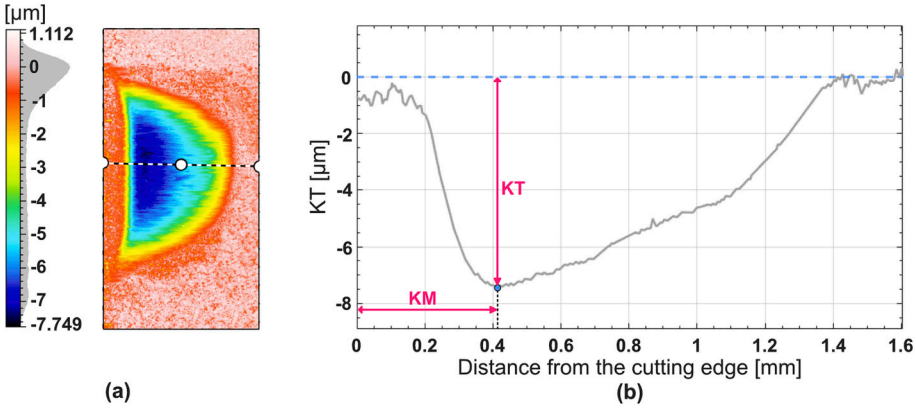

Fig. 2. **(a)** Examination of crater wear development on the rake face of the tool using an optical profilometer and **(b)** determination of the location of maximum crater wear depth (KM) along the line shown in (a). Orthogonal cutting of C50 steel at V_c=150 m/min and f=0.1 mm/rev.

Table 3
Experimental results obtained for orthogonal cutting of C50 steel. w = 2 mm.

Condition	V_c (m/min)	f (mm/rev)	F_c (N)	F_t (N)	l_c (mm)	t_c (mm)	KT (μm)	KM (mm)
1	100	0.1	611	564	1.50	0.32	2.28	0.436
2	150	0.1	602	572	1.48	0.30	7.41	0.427
3	200	0.1	573	503	1.20	0.29	11.42	0.381
4	250	0.1	555	454	1.05	0.29	16.79	0.395
5	300	0.1	538	414	0.95	0.28	22.56	0.438

material deformation behaviour encountered in the cutting zone. Essentially, the chip thickness ratio, rake angle and measured cutting forces would suffice for the estimation of stress and velocity in shear zones. This, in turn, allows for the estimation of the heat flux in the PSZ (q_{PSZ}) and at the tool-chip interface (q_{SSZ}) [18,19] using the following relationships:

$$q_{PSZ} = \eta \frac{F_s V_{sh}}{l_{sh} w} \tag{2}$$

$$q_{SSZ} = \eta \frac{F_f V_{ch}}{l_c w} \tag{3}$$

In these equations, η is the Taylor-Quinney coefficient determining the fraction of plastic strain energy density converted into heat [44]. F_s

and F_f are, respectively, the shear forces on the shear plane, i.e., the centreline of the PSZ, and the rake face of the tool. l_{sh} is the length of the shear plane and l_c is the contact length between the tool and chip, while w is the width of the cut. The shear velocity (V_{sh}) and chip velocity (V_{ch}) in Eqs. (2) and (3) are given as:

$$V_{sh} = \frac{cos\gamma}{cos(\phi - \gamma)} V_c \tag{4}$$

$$V_{ch} = \frac{sin\phi}{cos(\phi - \gamma)} V_c \tag{5}$$

In the above equations, γ is the rake angle, while ϕ represents the shear angle and is defined as:

$$tan\phi = \frac{r_c cos\gamma}{1 - r_c sin\gamma} \tag{6}$$

where $r_c = h_u/t_c$ represents the chip thickness ratio, i.e., the ratio between the uncut chip thickness (h_u) and the chip thickness (t_c) after the cutting process. The normal and shear forces acting on the rake face of the tool can be obtained from the measured cutting force (F_c) and feed force (F_t):

$$F_f = F_t cos\gamma + F_c sin\gamma \tag{7}$$

$$F_n = F_c cos\gamma - F_t sin\gamma \tag{8}$$

The shear force acting on the shear plane can then be obtained using the following equation:

$$F_s = \frac{cos(\phi + \lambda - \gamma)}{cos\lambda} F_n \tag{9}$$

λ in the above equation is called the friction angle, and it can be obtained using the measured forces as:

$$tan\lambda = \frac{F_t + F_c tan\gamma}{F_c - F_t tan\gamma} \tag{10}$$

In practice, however, the cutting edge is never entirely sharp. Instead, tools often include a rounded cutting-edge geometry. The deviation from the ideal cutting-edge geometry causes the process force to divide into a resultant force acting on the rake face of the tool and a ploughing force that is exerted on the rounded edge and a small portion of the adjacent flank surface [45,46]. This may suggest that the ploughing force component should be excluded when calculating the heat generated on the rake face of the tool [25].

3.2. Heat generation during chip formation – rounded cutting-edge geometry

The deviation from the ideal cutting-edge geometry alters the distribution of shear and normal forces on the rake face and thus affects both the intensity and distribution of generated heat on the tool surfaces. The material flow ahead of the rounded cutting edge is normally characterised by either a stagnation point or a ploughing zone [45]. The material above the stagnation point leaves with the chip, whereas the material under the stagnation point extends towards the machined surface, as shown in Fig. 3. The tractions around the edge due to the material flow under the stagnation point, as well as the elastic recovery of the material after the cutting, are the main reasons for ploughing force – also known as 'indentation force'. Generally, the ploughing effect accounts for a larger fraction of the feed force than the cutting force. The literature reports percentages of the ploughing effect ranging from 17 % to 58 % of the feed force and 5 % to 21 % of the cutting force [47]. Numerous studies have focused on determining the ploughing force using mechanistic and/or slip-line models. Denkena and Biermann [45] reviewed these attempts in detail.

The rounded cutting edge also causes the actual uncut chip thickness to be less than the corresponding theoretical value for the perfectly sharp cutting edge, thereby changing the shear angle. Here, the model proposed by Waldorf et al. [48] is used to obtain the actual uncut chip thickness and shear angle when cutting with a rounded cutting edge. Knowing the stagnation angle θ_s and the cutting-edge radius r_e, the ploughing depth can be obtained as:

$$h_p = r_e(1 - cos\theta_s) \tag{11}$$

Thus, the actual uncut chip thickness for a round cutting edge reduces to $h_a = h_u - h_p$, and the shear angle may be expressed using a more comprehensive relationship [48] compared to that of a perfectly sharp tool (see Eq. (5)):

$$\phi = tan^{-1}\left(\frac{h_u}{r_e tan\left(\frac{\pi}{4} + \frac{\gamma}{2}\right) + \frac{h_p}{tan\left(\frac{\pi}{2} + \gamma\right)} - \sqrt{2r_e h_p - h_p{}^2} + \frac{t_c}{cos\gamma} - h_u tan\gamma} \right) \tag{12}$$

To determine the ploughing force, the cutting geometry is divided into six regions (segments), as shown in Fig. 4. The shear and normal forces acting on each segment are determined by integrating the normal

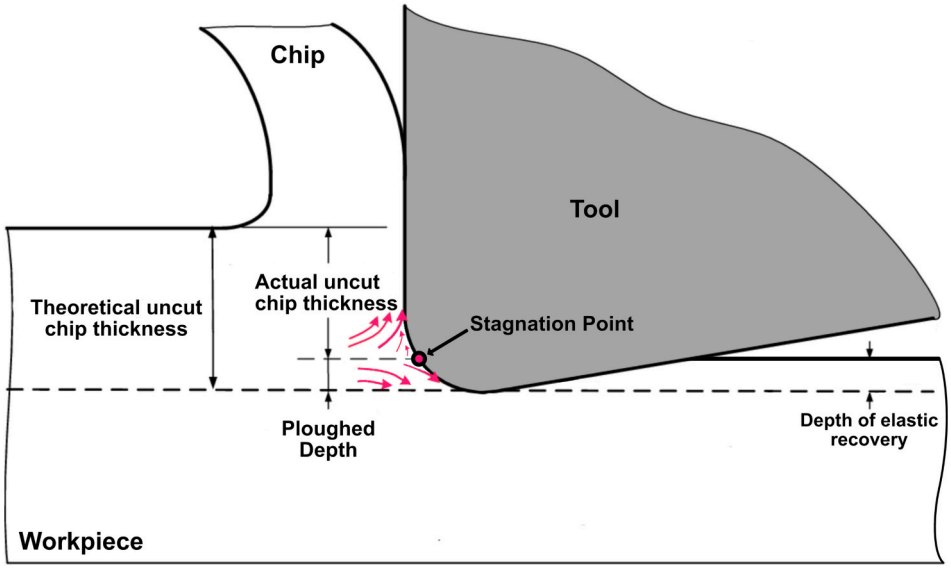

Fig. 3. Material flow near the rounded cutting edge resulting in a ploughing force.

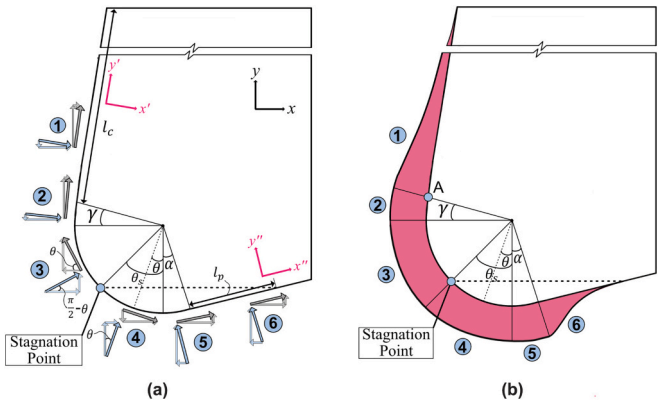

Fig. 4. **(a)** Division of the tool-chip and tool-workpiece contact regions into six segments allowing for determination of the ploughing force, **(b)** schematic distribution of normal stress along the tool-chip and too-workpiece contact regions.

pressure and shear stress distributions in regions 1 to 6. A similar approach is used by Çelebi et al. [39] and Budak et al. [40] to calculate the ploughing force. The cutting and feed forces are then calculated by adding the shear and normal force components projected along the cutting and feed directions, as shown in Fig. 4a. Here, the normal stress on the rake face is estimated using the following relationship [49]:

$$\sigma = \sigma_0 \left(1 - \frac{y'}{l_c}\right)^{\xi} \tag{13}$$

where σ_0 is the maximum pressure on the tool surface, y' is the distance on the rake face from point A (shown in Fig. 4b), and ξ is a constant. Eq. (13) is also used to estimate the decay of normal stress along the flank surface (region 6); however, the ploughing length on the flank face of the tool (l_p) is used instead of l_c. A similar exponential constant of $\xi = 3$ is used for both rake and flank surfaces. The same value is used by Ozlu et al. [49] to present the normal stress distribution on the rake face, in accordance with the experimental observations. The normal stress is assumed to be constant in regions 2 to 5, taking the maximum value of σ_0. Here, the shear stress distribution on the rake and clearance surfaces (regions 1 and 6) is simulated using a pressure-dependent shear friction model, as per Childs et al. [50] and Shirakashi and Usui [51]:

$$\tau = k_{ssz}(1 - e^{-n\sigma}) \tag{14}$$

In Eq. (13), k_{ssz} is the shear strength of the material in the SSZ, σ is the normal stress expressed by Eq. (13), while n is a constant taking a value between 0.0040 and 0.0045 for machining plain carbon steels using uncoated tools. Here, $n = 0.0045$ is used in accordance with the previous FE-based analyses of the frictional condition at the tool-chip interface [52,53]. As inferred from Fig. 4b and Eq. (14), the friction stress on the rake face near (and around) the cutting edge approaches the shear strength of the material, but it gradually decreases with increased distance from the cutting edge. Hence, Eq. (14) allows for simulation of the sticking-sliding frictional conditions on the rake face using a single mathematical expression.

The maximum normal stress (σ_0) and shear strength of the material in the secondary shear zone (k_{ssz}) can be obtained by minimising the difference between the cumulative cutting and feed forces (see Appendix I) and the corresponding measured values using an iterative approach. Once these two parameters are identified, the normal and shear forces acting on the rake face of the tool (i.e., F_n and F_f), and thus the constant heat flux in the PSZ and SSZ can be estimated by Eqs. (2) and (3).

3.3. Variable heat flux at tool-chip interface

Numerous studies have shown that the heat flux is not constant on the tool's rake face [4,6,54], and thus Eq. (3) only provides a primary estimation that is inconsistent with well-established tribological investigations. Experimental observations have revealed that the tool-chip interface consists of two regions: a sticking zone that is subjected to full seizure and a sliding zone where frictional sliding is predominant [20,38,49]. The tool-chip interface experiences full seizure near the cutting edge, where the workpiece material *welds* onto the tool's rake face surface due to extreme normal stresses exerted on the surface. This zone is believed to experience sticking friction and allows the heat from the plastic deformation to propagate into the tool through conduction [4]. The amount of heat generated due to the plastic work is proportional to the shear stress and shear strain rate to which the workpiece material is subjected near the interface [20,38]. In this region, shear stress (τ) reaches the shear strength of the workpiece material (k_{ssz}), as inferred from Eq. (14). The sliding zone, on the other hand, exhibits a relative motion between the chip and the tool. Therefore, the distributions of sliding velocity and shear stress at the interface determine the heat generation in this region [38]. There should, however, be a transition region between these two zones to maintain material continuity at the tool-chip interface [38], as shown in Fig. 5. This zone is characterised by a combination of sticking and sliding friction, and thus both mechanisms are responsible for heat generation in the transition region. Following the above arguments, the heat flux at the tool-chip interface (q_{SSZ}) can be expressed using Eq. (15):

$$q_{SSZ} = \begin{cases} \dfrac{1}{2}\delta\dot{\gamma}\tau & \text{for } 0 \le y \le l_{st} \\ \dfrac{1}{2}\delta\dot{\gamma}\tau\left(1 - \dfrac{V_{\chi,\psi}}{V_{ch}}\right) + \tau V_{\chi,\psi} & \text{for } l_{st} \le y \le l_{st} + l_{tr} \\ \tau V_{\chi,\psi} & \text{for } l_{st} + l_{tr} \le y \le l_c \end{cases} \tag{15}$$

In Eq. (15), $\dot{\gamma}$ is the shear strain rate and $V_{\chi,\psi}$ is the velocity distribution at the tool-chip interface. l_{st} and l_{tr} are the length of the sticking and transition regions, respectively; y is the distance from the cutting edge; and δ represents the maximum thickness of the SSZ, as shown in Fig. 5. It is also worth stressing here that $V_{\chi,\psi} = 0$ in the sticking zone and $V_{\chi,\psi} = V_{ch}$ in the sliding zone (l_{sl} in Fig. 5).

The fraction of the interface occupied by each of these three zones depends on the cutting conditions and properties of the workpiece and tool materials involved [49]. The variation in the length of the sliding and sticking regions has a direct impact on the thermal conduction path between the tool and the chip [4]. In addition, it determines the amount of heat generated along the tool-chip interface according to Eq. (15). Nevertheless, the velocity distribution near the interface in the SSZ needs to be known to estimate the heat shear strain rate. The velocity distribution at the tool-chip interface, $V_{\chi,\psi}$, can be given as a function of both x- and y- coordinates as [38]:

$$V_{\chi,\psi} = V_{ch}(\chi - \chi\psi + \psi)^{\frac{1}{4}}, \text{for } 0 \le x \le \delta \text{ and } 0 \le y \le l_c \tag{16}$$

In Eq. (16), χ, ψ and κ are non-dimensional local coordinates defined as:

$$\chi = \frac{\varrho y^{\varsigma}}{\Omega^{\varsigma} + y^{\varsigma}} \tag{17a}$$

$$\kappa = \frac{y}{l_{st} + l_{tr}} \tag{17b}$$

$$\psi = \frac{x}{\delta(1 - \kappa)} \tag{17c}$$

Here, $\varrho = 1$, $\varsigma = 25$ and $\Omega = l_{st} + l_{tr}/2$ are assumed to ensure a smooth transition between the sticking and sliding zones.

The shear strain rate $\dot{\gamma}$ at a given location within the SSZ can then be

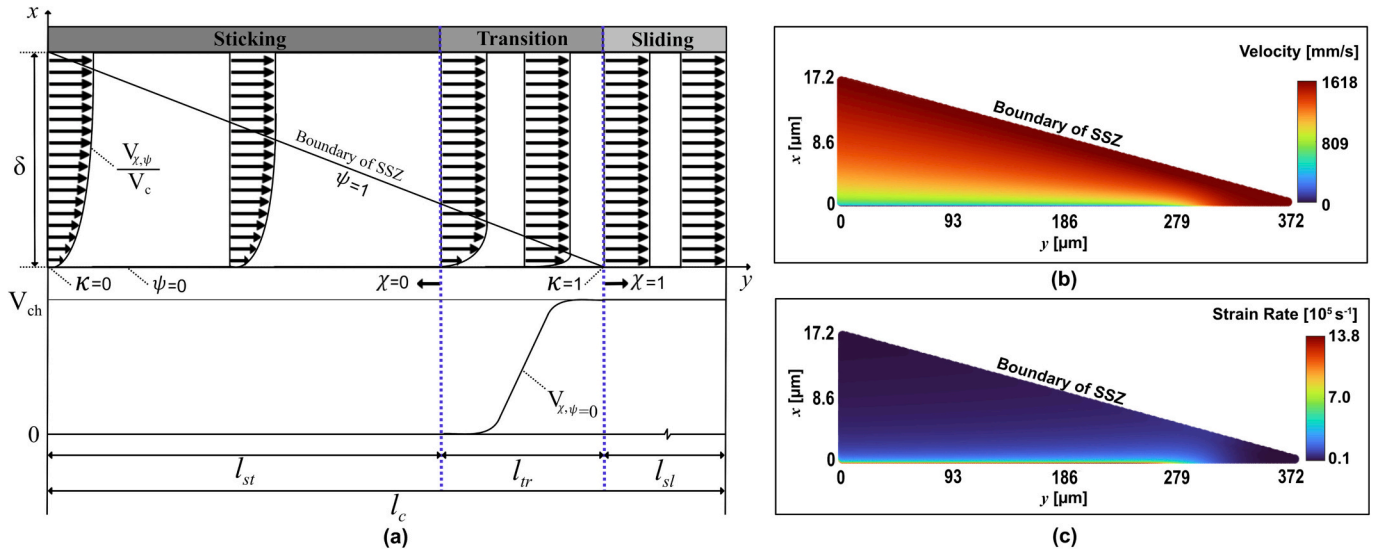

Fig. 5. **(a)** Schematic variation of velocity profile in the sticking (l_{st}), transition (l_{tr}) and sliding (l_{sl}) regions; **(b)** velocity profile in the secondary shear zone as obtained for the case of C45 steel (V_c=200 m/min and f=0.2 mm/rev) with a mesh grid of 500 discrete points; and **(c)** strain rate profile in the secondary shear zone as obtained for the case of C45 steel (V_c=200 m/min and f=0.2 mm/rev) with a mesh grid of 500 discrete points.

calculated as (see Appendix II):

$$\dot{\gamma} = \frac{1}{4}\frac{V_{ch}(1-\chi)}{\delta(1-\kappa)}\left(\frac{V_{\chi,\psi}}{V_{ch}}\right)^{-3} \tag{18}$$

The velocity distribution and calculated shear strain rate within the SSZ are shown in Fig. 5b and c. Incorporating the physics-based distributions for velocity (Eq. (16)) and shear stress (Eq. (14)) at the tool-chip interface, as shown in Fig. 6a, along with the average shear strain rate in the SSZ (i.e., the mean value of all discrete shear strain rates obtained by Eq. (18) for $x > 0$) allows for estimation of variable heat flux on the rake face according to Eq. (15). Fig. 6b shows the total heat flux along the tool-chip interface as well as the heat contributions from the sticking and sliding zones for a given cutting condition. as: is evident, the maximum contribution of heat flux lies immediately after the transition region, where both the plastic deformation from the sticking zone and the frictional heat from the sliding zone are superposing to maximise the heat flux in that region. This variable heat flux is integrated into Komanduri and Hou's and Moufki et al.'s models, as will be discussed in Sections 4.1 and 4.2.

4. Semi-analytical cutting temperature models

4.1. Komanduri and Hou's model

Komanduri and Hou's model, referred to as Model I in this study, is a well-established semi-analytical model that has broadly been used in literature for the prediction of tool, chip and workpiece temperature during dry machining in two dimensions, i.e., orthogonal cutting [18,21,22]. This model assumes uniform heat generation in the PSZ and SSZ but adopts a non-uniform heat partition distribution between the tool and chip along the tool-chip interface.

Komanduri and Hou's temperature analysis is done in three separate parts: (a) the workpiece, (b) the chip and (c) the cutting tool with an ideal edge, which are then combined to obtain the overall temperature

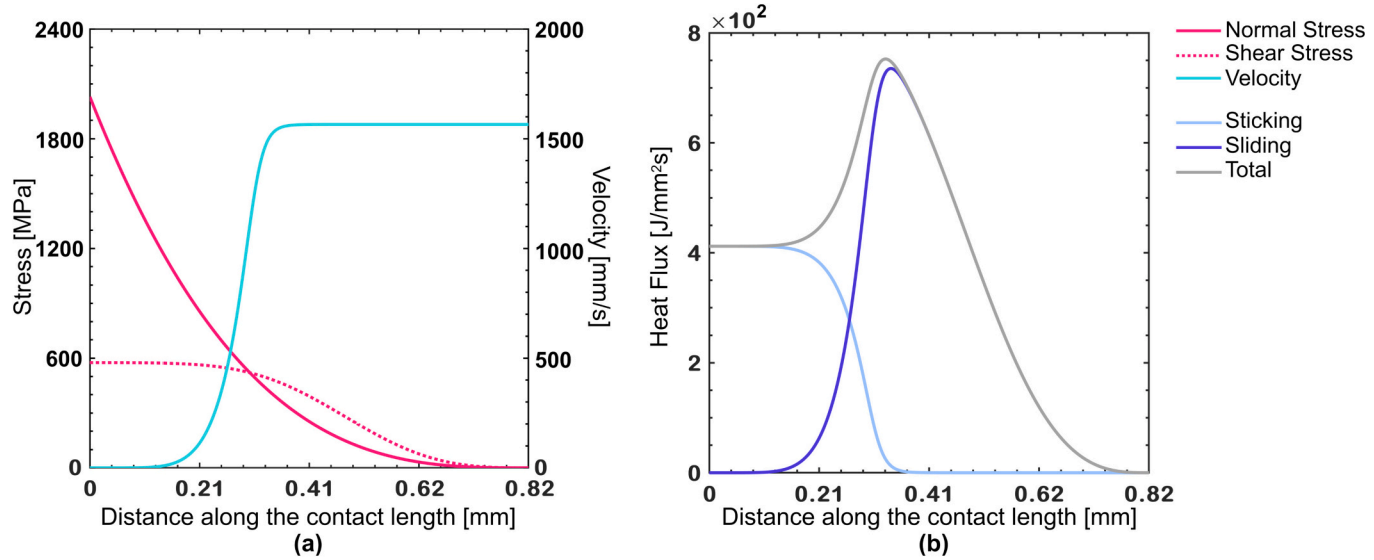

Fig. 6. (a) Velocity and stress distributions along the tool-chip interface for the case of C45 steel (V_c=200 m/min and f=0.2 mm/rev) and (b) the resulting contributions of heat flux from the sticking and sliding zones along the contact length for an ideal cutting edge.

distributions within each part. Here, only the chip and the tool are considered. This model includes two heat sources for temperature calculation in either the chip or the tool, one representing the temperature rise due to the heat generated in the PSZ and the other representing the heat generated at the tool-chip interface. The authors applied a common coordinate system for each region and set adiabatic boundary conditions with image heat sources to predict the temperature increase in the tool and chip during the machining process. The temperature increase due to the heat generation in the PSZ is then calculated using a modified Hahn's solution for a moving oblique band heat source in a semi-infinite medium for both the primary shear plane and its image heat sources, as shown in Fig. 7.

These result in two sets of equations for the chip, one representing the temperature increase due to the PSZ and the other representing the temperature increase due to heat generation in the SSZ. The temperature increase in the chip due to the PSZ ($\Delta T_{chip,PSZ}$) is calculated using the following expression [22]:

$$\Delta T_{chip,PSZ} = \frac{q_{PSZ}}{2\pi k_w}\left[\int_0^{l_{sh}} e^{-(y-l_i sin(\phi-\gamma))\frac{V_{ch}}{2\alpha_w}}\left[K_0\left(R_1\frac{V_{ch}}{2\alpha_w}\right)+K_0\left(R_1^{'}\frac{V_{ch}}{2\alpha_w}\right)\right]\mathrm{d}l_i\right] \tag{19}$$

with $R_1 = \sqrt{(y-l_i sin(\phi-\gamma))^2+(x-l_i cos(\phi-\gamma))^2}$ and $R_1^{'} = \sqrt{(y-l_i sin(\phi-\gamma))^2+(x+l_i cos(\phi-\gamma))^2}$.

In Eq. (19), q_{PSZ} is the heat liberation intensity of a moving-band heat source, k_w and α_w are respectively the thermal conductivity and diffusivity of the workpiece, and K_0 is the modified Bessel function of second kind – zero order. Here, R_1 and $R_1^{'}$ are the distances between the moving line heat source and the point M at which the temperature is being calculated. x and y are the coordinates of point M with reference to the system shown in Fig. 7, while l_i is the position of the differential segment of the band heat source dl_i.

The temperature increase due to the SSZ is evaluated based on a modified Jaeger's solution for a moving-band heat source for the chip and a stationary rectangular heat source for the tool. The schematic representation of these heat sources is shown in Fig. 8. Hence, the temperature increase in the chip due to the plastic work and frictional heat source at the tool-chip interface, $\Delta T_{chip,SSZ}$, is obtained using Eq. (20) [22]:

$$\Delta T_{chip,SSZ} = \frac{q_{SSZ}}{\pi k_w}\left[\begin{array}{l}(B_{chip}-\Delta B)\int_0^{l_c} e^{-(y-l_i)\frac{V_{ch}}{2\alpha_w}}\left[K_0\left(R_2\frac{V_{ch}}{2\alpha_w}\right)+K_0\left(R_2^{'}\frac{V_{ch}}{2\alpha_w}\right)\right]\mathrm{d}l_i \\ +2\Delta B\int_0^{l_c}\left(\frac{l_i}{l_c}\right)^m e^{-(y-l_i)\frac{V_{ch}}{2\alpha_w}}\left[K_0\left(R_2\frac{V_{ch}}{2\alpha_w}\right)+K_0\left(R_2^{'}\frac{V_{ch}}{2\alpha_w}\right)\right]\mathrm{d}l_i \\ +C\Delta B\int_0^{l_c}\left(\frac{l_i}{l_c}\right)^k e^{-(y-l_i)\frac{V_{ch}}{2\alpha_w}}\left[K_0\left(R_2\frac{V_{ch}}{2\alpha_w}\right)+K_0\left(R_2^{'}\frac{V_{ch}}{2\alpha_w}\right)\right]\mathrm{d}l_i\end{array}\right] \tag{20}$$

with $R_2 = \sqrt{(y-l_i)^2+x^2}$ and $R_2^{'} = \sqrt{(y-l_i)^2+(2t_c-x)^2}$ where B_{chip}, ΔB, m, k and C are functional parameters, whose identification procedure will be discussed later in this section. R_2 and $R_2^{'}$ are respectively the distances between the interface and image heat source and the point M at which the temperature is being calculated. Here, l_i is the position of the differential segment of the heat source dl_i along the tool-chip interface, as shown in Fig. 8. With reference to the same figure, the temperature increase in the tool due to the heat generation occurring in the SSZ can be calculated using Eq. (21) [22]:

$$\Delta T_{tool,SSZ} = \frac{q_{SSZ}}{2\pi k_t}\left[\begin{array}{l}(B_{tool}+\Delta B)\int_{-w/2}^{+w/2}\int_0^{l_c}\left(\frac{1}{R_3}+\frac{1}{R_3^{'}}\right)\mathrm{d}y_i\mathrm{d}z_i \\ -2\Delta B\int_{-w/2}^{+w/2}\int_0^{l_c}\left(\frac{y_i}{l_c}\right)^m\left(\frac{1}{R_3}+\frac{1}{R_3^{'}}\right)\mathrm{d}y_i\mathrm{d}z_i \\ -C\Delta B\int_{-w/2}^{+w/2}\int_0^{l_c}\left(\frac{y_i}{l_c}\right)^k\left(\frac{1}{R_3}+\frac{1}{R_3^{'}}\right)\mathrm{d}y_i\mathrm{d}z_i\end{array}\right] \tag{21}$$

with $R_3 = \sqrt{x^2+(y-y_i)^2+(z-z_i)^2}$ and $R_3^{'} = \sqrt{x^2+(y-2l_c+y_i)^2+(z-z_i)^2}$.

In this equation, B_{tool} is a functional parameter to be determined,

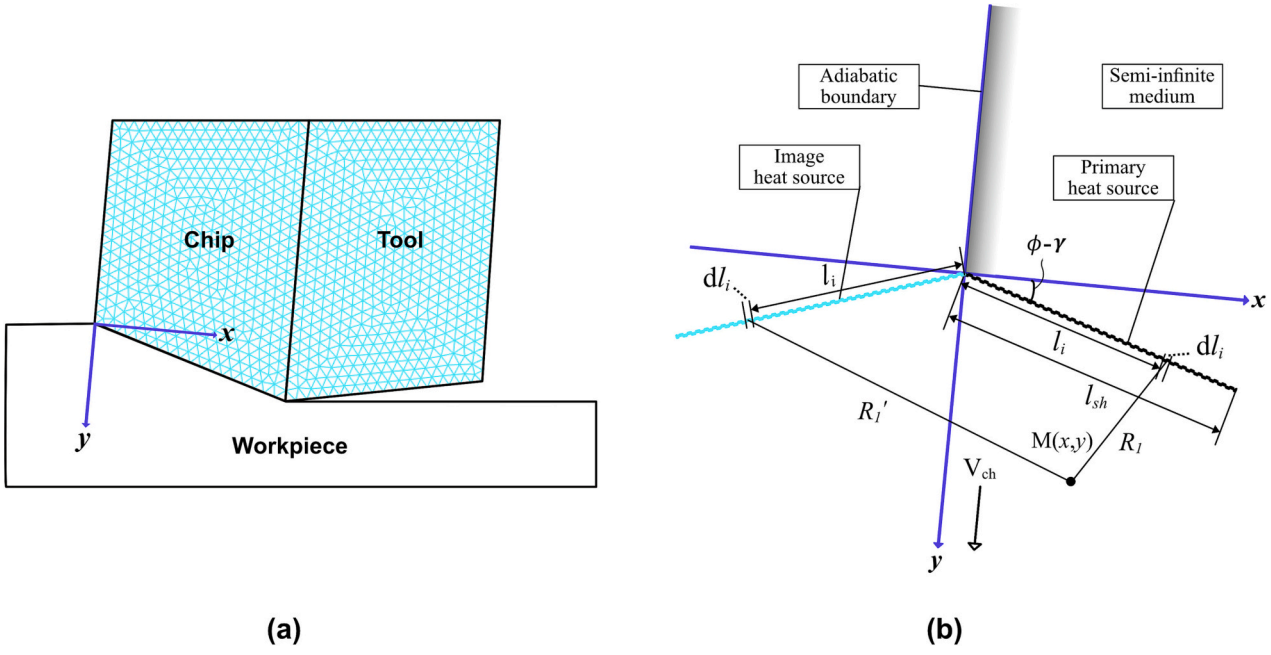

Fig. 7. Schematic representation of the primary shear plane and its image heat sources based on the model by Komanduri and Hou [18,21,22].

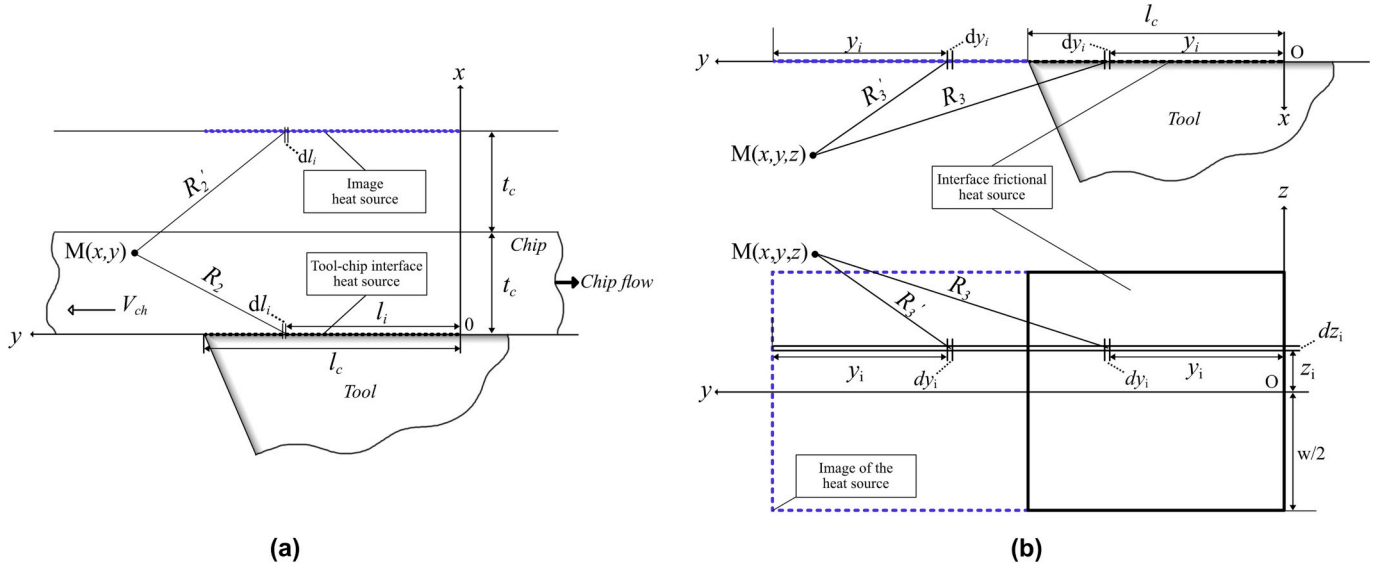

Fig. 8. Schematic representation of the SSZ and its image heat sources for **(a)** the chip side and **(b)** the tool side based on the model by Komanduri and Hou [18,21,22].

while z and z_i are the coordinates of the point M and the differential heat source in the z-direction respectively. Here, z is set to zero to obtain R_3 and $R_3^{'}$, since the calculation is done in 2D. The heat liberation intensity (q_{SSZ}) in Eqs. (20) and (21) may be assumed to be constant or variable according to Eqs. (3) and (15), respectively. The continuity of heat flow requires the temperature distribution at the tool-chip interface to be consistent on both the chip and tool sides. To achieve this, Komanduri and Hou applied an imaginary rectangular heat source, referred to as an induced heat source, to account for the fraction of heat flowing from the PSZ into the tool. The temperature rise in the tool due to the PSZ is thus calculated as:

$$\Delta T_{tool,PSZ} = \frac{q_{pli}}{2\pi k_t}\begin{bmatrix} \left(B_{ind}+\Delta\widetilde{B}\right)\int_{-w/2}^{+w/2}\int_{0}^{l_c}\left(\frac{1}{R_3}+\frac{1}{R_3^{'}}\right)\mathrm{d}y_i\mathrm{d}z_i \\ -2\Delta\widetilde{B}\int_{-w/2}^{w/2}\int_{0}^{l_c}\left(\frac{y_i}{l_c}\right)^{\widetilde{m}}\left(\frac{1}{R_3}+\frac{1}{R_3^{'}}\right)\mathrm{d}y_i\mathrm{d}z_i \\ -\widetilde{C}\Delta\widetilde{B}\int_{-w/2}^{w/2}\int_{0}^{l_c}\left(\frac{y_i}{l_c}\right)^{\widetilde{k}}\left(\frac{1}{R_3}+\frac{1}{R_3^{'}}\right)\mathrm{d}y_i\mathrm{d}z_i \end{bmatrix} \quad (22)$$

with $R_3 = \sqrt{x^2+(y-y_i)^2+(z-z_i)^2}$ and $R_3^{'} = \sqrt{x^2+(y-2l_c+y_i)^2+(z-z_i)^2}$.

Here, q_{pli}, $\Delta\widetilde{B}$, $\widetilde{m}$, $\widetilde{k}$ and $\widetilde{C}$ are functional parameters associated with the induced heat source and $B_{ind} = 1$. Nevertheless, the functional parameters in Eqs. (20)–(22), namely, m, k, C, $\widetilde{m}$, $\widetilde{k}$, $\widetilde{C}$, q_{pli}, ΔB, $\Delta\widetilde{B}$ and B_{tool}, are directly linked to the non-uniform heat partitioning between the chip and the tool [22] and determine whether the temperature distribution between the chip and tool coincides at the interface. It should be noted here that $B_{chip} = 1 - B_{tool}$. Komanduri and Hou determined these parameters by using functional analysis; however, their approach is time-consuming, prone to error and not easily adaptable for new workpiece-tool combinations.

To overcome this limitation, an ML-based (machine learning–based) approach is developed to determine these functional parameters in a consistent manner for both Models I (C) and I (V). The methodology adopted to optimise the functional parameters relies on training an ML model to predict the value of an objective function based on a given set of ten functional parameters. The mean squared error was used as the objective function:

$$g(X_j) = \frac{1}{N}\sum_{i=1}^{N}\left(T_{chip,i}(X_j) - T_{tool,i}(X_j)\right)^2 \quad (23)$$

Here, X_j is the j^{th} vector including a given set of functional parameters from Eqs. (20)–(22), N is the number of discrete points at the tool-chip interface (determined by the mesh density), and $T_{chip,i}$ and $T_{tool,i}$ are respectively the temperatures on the chip and tool sides at each discrete point i. In the case of Model I (C), the vector X_j includes the ten functional parameters, m, k, C, $\widetilde{m}$, $\widetilde{k}$, $\widetilde{C}$, q_{pli}, ΔB, $\Delta\widetilde{B}$ and B_{tool}. For Model I (V), the functional parameters are reduced to five so that the vector X_j consists of m, k, C, ΔB and B_{tool}. Noteworthily, the functional parameter q_{pli}, which denotes the heat flux of the induced plane heat source in the primary shear zone, is no longer required to calculate the temperature rise on the tool for Model I (V) when q_{SSZ} in Eq. (21) is calculated using the physics-based expression given in Eq. (15). The value of the objective function is indicative of the deviation between the temperatures obtained at the discrete points on the tool and chip sides to be minimised. An appropriate ML model is trained to establish the relationship between the functional parameters and the objective function. Once this relationship is obtained, the optimum set of parameters can be determined using various optimisation strategies. This methodology is illustrated in the schematic shown in Fig. 9.

A total of 1000 randomised sets of functional parameters were generated to calculate the temperature at the tool-chip interface on both the chip and tool sides. Each parameter was varied within a predetermined range reported in the literature [22]. The objective function was then calculated for each of the 1000 sets. Of those, 800 sets were used for training different Gaussian process regression models, including rational quadratic, exponential, squared exponential, Matérn 5/2 and Matérn 3/2 kernel (covariance) functions [55]. Of these, the regression model that exhibited the best performance upon cross-validation (i.e., using the remaining 200 sets) was the Gaussian regression with the squared exponential kernel function. If the validation of the obtained model was successful, i.e., its R-squared value was higher than 0.95, then the trained model was accepted and subject to optimisation. If the R-squared value was lower than 0.95, the ML model was recalibrated, and the process was repeated until a satisfactory model was obtained. Once the ML model was accepted, the minimisation of the objective function was performed using the interior point optimisation

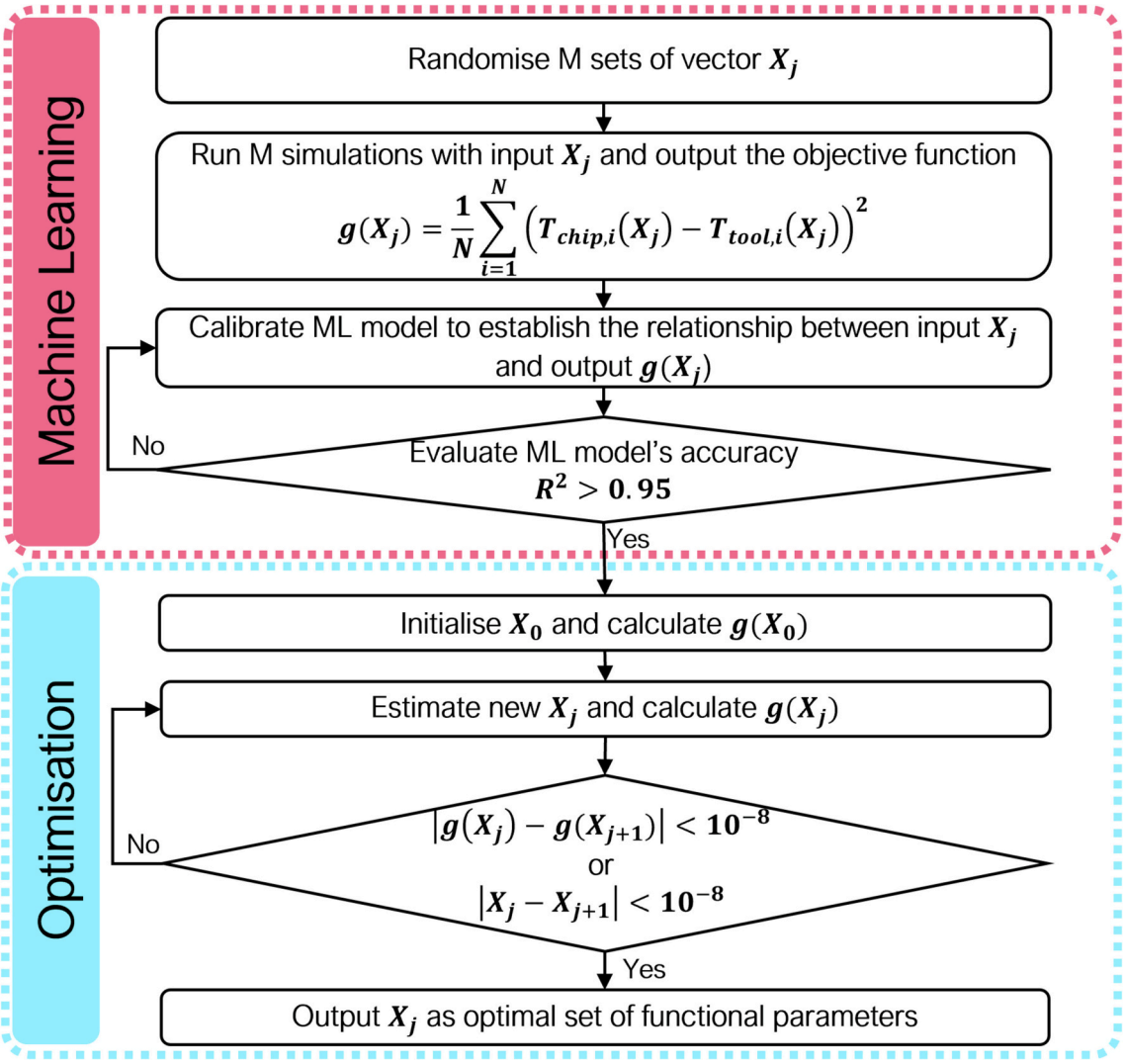

Fig. 9. Flowchart detailing the machine learning model (calibration and validation) and the optimisation of functional parameters in the Komanduri and Hou models based on the minimisation of a constrained nonlinear multivariable objective function.

algorithm to yield the set of parameters that produced the optimal match between both sides of the tool-chip interface [55]. This algorithm outperformed the other tested algorithms, including the genetic, particle swarm and pattern search algorithms [55]. It should be mentioned here that this approach did not always yield satisfactory results, and careful selection of optimisation constraints (parameter boundaries) and initial guessing were required to ensure a sufficiently close match at the tool-chip interface, particularly for the cases where variable heat source was incorporated. However, this approach allows for a more efficient determination of functional parameters when a new cutting condition and/or tool-material combination are investigated.

4.2. Moufki et al.'s model

Wright et al. [19] proposed a solution for the conductive-advection equation (Eq. (1a)) to predict the temperature distribution at the tool-chip interface. Later, Moufki et al. [20] extended this model, here referred to as Model II, to obtain the temperature distribution within the entire chip domain. This solution relies on the assumption that heat conduction in the chip flow direction is negligible, which simplifies the conductive-advection differential equation, Eq. (1a):

$$-\frac{\partial T}{\partial y} + \frac{\alpha_w}{V_{ch}}\frac{\partial^2 T}{\partial x^2} = 0 \tag{24}$$

This equation is solved using an appropriate Laplace transform to determine the temperature within the chip [20] and/or at the tool-chip interface [19]. The boundary conditions associated with Eq. (24) are illustrated in Fig. 10. As is evident, $T(x, y = 0) = 0$, which means that the presented solution results in zero temperature at the cutting edge in the absence of a PSZ heat source. Hence, the temperature rise estimation at the interface and within the chip requires the average temperature in the PSZ ($\bar{T}_{PSZ}$) to be known:

$$\Delta T_{chip} = \bar{T}_{PSZ} + \frac{1}{k_w}\sqrt{\frac{\alpha_w}{\pi V_{ch}}}\int_0^{l_c} B_{chip} q_{SSZ}(y - z)\frac{1}{\sqrt{z}} exp\left(\frac{-V_{ch}x^2}{4\alpha_w z}\right) dz \tag{25}$$

In Eq. (25), $\bar{T}_{PSZ}$ is the average temperature at the primary shear plane. In this equation, heat liberation intensity at the tool-chip interface (q_{SSZ}) can be assumed to be constant (Eq. (3)) or variable (Eq. (15)), referred to as Model II (C) and Model II (V), respectively.

Wright et al. [19] and Moufki et al. [20] implemented various methods to obtain the average temperature in the PSZ. In this study, Eq. (19) is used to determine the average temperature $\bar{T}_{PSZ}$ required to obtain the temperature distribution within the chip according to Eq.

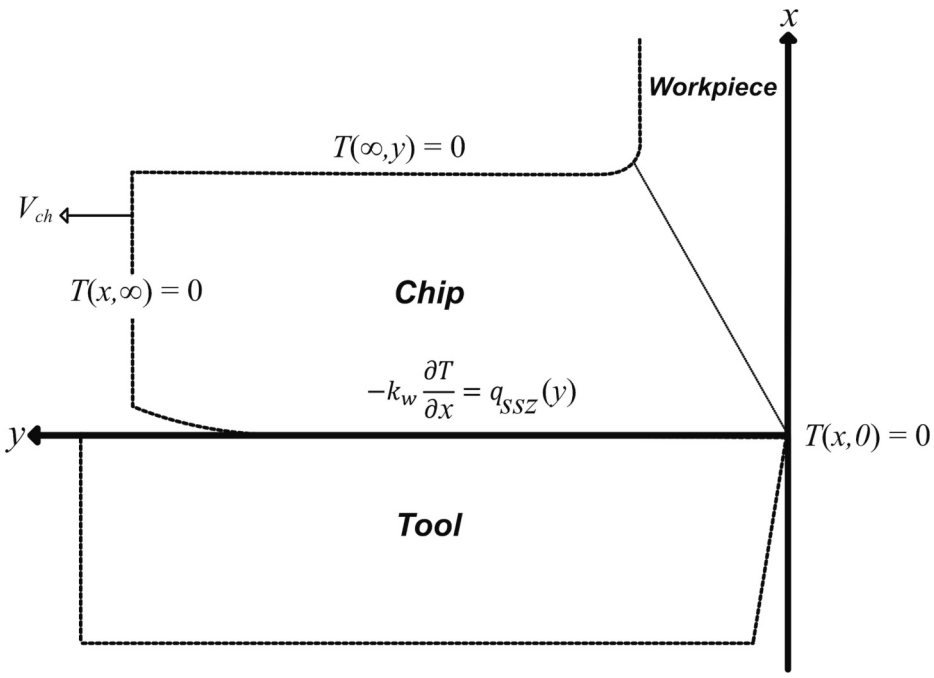

Fig. 10. Schematic representation of boundary conditions used in the model by Wright et al. [19] and Moufki et al. [20].

(25). Nevertheless, unlike in Komanduri and Hou's model, a priori knowledge of the heat partition coefficient is still needed for estimation of temperature distribution using this model. This is because this model solely estimates the temperature within the chip, which prevents the identification of the heat partition coefficient by matching the temperature distributions at the interface. Wright et al. [19] and Moufki et al. [20], respectively, assumed 80 % and 100 % of heat partitions in the chip regardless of the cutting conditions involved. There are, however, numerous expressions proposed in the literature concerning heat partitioning in metal cutting, three of which are presented in Table 4. These equations are assessed to determine the most reliable heat partition coefficient for temperature estimation when machining plain carbon steels using uncoated cemented carbide tools under various cutting conditions.

5. Results and discussion

The merit of each model in this research is assessed based on its ability to predict the value of the maximum temperature as well as its location. The experimental results obtained from running the cutting conditions for C45 steel are used to validate the models' capabilities in predicting the maximum temperature using thermographic temperature measurements reported for the same tool-workpiece material combinations as in the literature [41]. Additionally, the results for C50 steel are used to assess the model's capability in predicting the location of this maximum temperature. The results obtained for an ideal cutting-edge geometry are presented in Section 5.1, while those obtained for a rounded cutting-edge geometry are presented in Section 5.2. Lastly, the sensitivity of the enhanced model to specific model parameters is discussed in Section 5.3.

Table 4
Equations used to evaluate the heat partition into the chip.

Reference	Equation
Berliner and Krajnov [56]	$B_{chip} = 1 - \dfrac{0.45\frac{k_t}{k_w}\sqrt{\frac{\pi\alpha_w}{V_{ch}l_c}}}{1+0.45\frac{k_t}{k_w}\sqrt{\frac{\pi\alpha_w}{V_{ch}l_c}}}$
List et al. [57]*	$B_{chip} = 1 - \dfrac{0.754\left(\frac{k_t}{k_w}/A_a\right)\sqrt{\frac{\alpha_w}{V_{ch}l_c}}}{1+0.754\left(\frac{k_t}{k_w}/A_a\right)\sqrt{\frac{\alpha_w}{V_{ch}l_c}}}$
Shaw and Cookson [58] **	$B_{chip} = 1 - \dfrac{0.754\frac{k_t}{k_w}A_a^{'}\sqrt{\frac{V_{ch}l_c}{2\alpha_w}}}{1+0.754\frac{k_t}{k_w}A_a^{'}\sqrt{\frac{V_{ch}l_c}{2\alpha_w}}}$

*, **: A_a and $A_a^{'}$ are geometric factors.

5.1. Ideal cutting edge

The main findings of each model for C45 and C50 steel using an ideal edge are summarised in Tables 5 and 6, respectively. For C45, since the crater wear profiles were unknown, the sticking length l_{st} was assumed to be 25 % greater than the feed. In contrast, for C50, the tool crater wear profiles were known; thus, the sticking length l_{st} could be estimated as the distance between the cutting edge and the onset of crater wear. For machining both steels using uncoated carbides, the transition length, l_{tr}, was estimated to be half of the sticking length.

The thermal properties of C45 steel and its corresponding tool were obtained from [41] by calculating the average of the reported temperature-dependent values over the temperature range 20–700°C. The thermal conductivity and diffusivity were defined as 29.06 W/m.K and 6.54 mm^2/s respectively, while the tool's properties were 65.00 W/m.K and 10.40 mm^2/s [41]. In the case of C50 steel and its corresponding tool, the thermal properties were obtained by means of JMatPro™ commercial software [59,60]. The thermal conductivity and diffusivity for C50 were defined as 34.66 W/m·K and 7.25 mm^2/s, while the tool's thermal properties were 77.89 W/m·K and 20.76 mm^2/s. The workpiece temperature is assumed to be 25°C for all cases. For all modified models, the stagnation angle θ_s was assumed to be 30° based on values available in the literature [41]. The selection of θ_s was also the focus of a sensitivity analysis, discussed in Section 5.3. Similarly, for all cutting conditions, the maximum thickness of the secondary shear zone δ was assumed to be 17.2 μm [61], noting that a sensitivity analysis within the range of values reported in the literature [61] showed that it has no significant impact on the temperature profile.

Table 5
Main findings of the different models for all cutting conditions of C45 steel using an ideal cutting edge.

Model	Cutting condition	ϕ (°)	l_{st} [a] (mm)	l_{tr} [b] (mm)	σ_0 (MPa)	k_{SSZ} (MPa)	$T_{C,max}$ (°C)	$T_{T,max}$ (°C)	B_{chip} (–)	$\bar{T}_{PSZ}$ (°C)
Model I (C)	1	17.7 ± 0.5	–	–	–	–	637 ± 17	636 ± 4	0.57	–
	2	21.8 ± 0.2	–	–	–	–	692 ± 0.3	694 ± 16	0.60	–
	3	22.8 ± 1.3	–	–	–	–	835 ± 10	827 ± 14	0.75	–
	4	26.8 ± 0.8	–	–	–	–	945 ± 2	938 ± 9	0.75	–
Model I (V)	1	17.7 ± 0.5	0.125	0.0625	2508 ± 389	978 ± 21	641 ± 34	639 ± 37	0.50	–
	2	21.8 ± 0.2	0.250	0.1250	2177 ± 196	773 ± 26	717 ± 19	716 ± 16	0.56	–
	3	22.8 ± 1.3	0.125	0.0625	1759 ± 75	772 ± 3	901 ± 3	898 ± 2	0.57	–
	4	26.8 ± 0.8	0.250	0.1250	2113 ± 83	657 ± 12	914 ± 19	916 ± 17	0.63	–
Model II (C)	1	17.7 ± 0.5	–	–	–	–	924 ± 15	–	0.77	385 ± 5
	2	21.8 ± 0.2	–	–	–	–	969 ± 0.1	–	0.80	325 ± 5
	3	22.8 ± 1.3	–	–	–	–	1076 ± 8	–	0.85	331 ± 10
	4	26.8 ± 0.8	–	–	–	–	1188 ± 3	–	0.86	291 ± 9
Model II (V)	1	17.7 ± 0.5	0.125	0.0625	2508 ± 389	978 ± 21	881 ± 33	–	0.77	385 ± 5
	2	21.8 ± 0.2	0.250	0.1250	2177 ± 196	773 ± 26	927 ± 21	–	0.80	325 ± 5
	3	22.8 ± 1.3	0.125	0.0625	1760 ± 75	772 ± 3	1097 ± 1	–	0.85	331 ± 10
	4	26.8 ± 0.8	0.250	0.1250	2113 ± 83	657 ± 12	1110 ± 17	–	0.86	291 ± 9

[a] $l_{st} = 1.25f$.
[b] $l_{tr} = 0.5l_{st}$

Table 6
Main findings of the different models for all cutting conditions of C50 steel using an ideal cutting edge.

Model	Cutting condition	ϕ (°)	l_{st} (mm)	l_{tr} [a] (mm)	σ_0 (MPa)	k_{SSZ} (MPa)	$T_{C,max}$ (°C)	$T_{T,max}$ (°C)	B_{chip} (–)	$\bar{T}_{PSZ}$ (°C)
Model I (C)	1	17.3	–	–	–	–	502	526	0.68	–
	2	18.4	–	–	–	–	585	601	0.74	–
	3	19.0	–	–	–	–	642	632	0.77	–
	4	19.0	–	–	–	–	690	682	0.80	–
	5	19.6	–	–	–	–	726	719	0.81	–
Model I (V)	1	17.3	0.19	0.095	814	444	519	516	0.51	–
	2	18.4	0.17	0.085	813	457	658	664	0.53	–
	3	19.0	0.15	0.075	955	464	737	740	0.55	–
	4	19.0	0.12	0.060	1057	460	799	801	0.60	–
	5	19.6	0.09	0.045	1133	453	865	864	0.64	–
Model II (C)	1	17.3	–	–	–	–	692	–	0.77	371
	2	18.4	–	–	–	–	790	–	0.81	354
	3	19.0	–	–	–	–	856	–	0.83	347
	4	19.0	–	–	–	–	903	–	0.85	348
	5	19.6	–	–	–	–	942	–	0.86	343
Model II (V)	1	17.3	0.19	0.095	814	444	732	–	0.77	371
	2	18.4	0.17	0.085	813	457	850	–	0.81	354
	3	19.0	0.15	0.075	955	464	924	–	0.83	347
	4	19.0	0.12	0.060	1057	460	988	–	0.85	348
	5	19.6	0.09	0.045	1132	452	1050	–	0.86	343

[a] $l_{tr} = 0.5l_{st}$

In Tables 5 and 6, $T_{C,max}$ and $T_{T,max}$ are respectively the maximum temperatures obtained along the interface on the chip and tool sides. $\bar{T}_{PSZ}$, the average temperature at the primary shear zone necessary to obtain the overall temperature distribution within the chip by Models II (C) and (V), is also given in these tables (see Section 4.2). For Models I (C) and (V), the values of $\bar{T}_{PSZ}$ are not reported, given that those models do not add the average value $\bar{T}_{PSZ}$, but instead use the node-by-node value of $T_{chip,PSZ}$ (see Eq. (19)). For Models I (C) and (V), the value of B_{chip} was obtained using the ML-based optimisation algorithm discussed in Section 4.1 to secure the best match between the temperature profiles on the chip and tool sides.

The values of B_{chip} reported for Models II (C) and (V) correspond to the values obtained using the Shaw and Cookson equation in Table 4. Fig. 11 shows the comparison between the estimated B_{chip} using the equations shown in Table 4, along with the maximum interface temperature predicted using Model II (V). The equation by Berliner and Krajnov predicted a B_{chip} value between 0.84 and 0.95, List et al. between 0.84 and 0.89, and lastly, Shaw and Cookson between 0.76 and 0.86 for the conditions used in this study. Despite compliance with general experimental trends [62], the estimated heat partitioning coefficients resulted in an overestimation of the maximum temperature for all investigated cutting conditions, especially at the lower cutting speeds as shown in Fig. 11b. The average error percentages obtained for the estimation of the maximum temperature using Model II (V) are 37 %, 44 % and 35 % using the Berliner and Krajnov, List et al., and Shaw and Cookson equations, respectively. Similarly, the average error

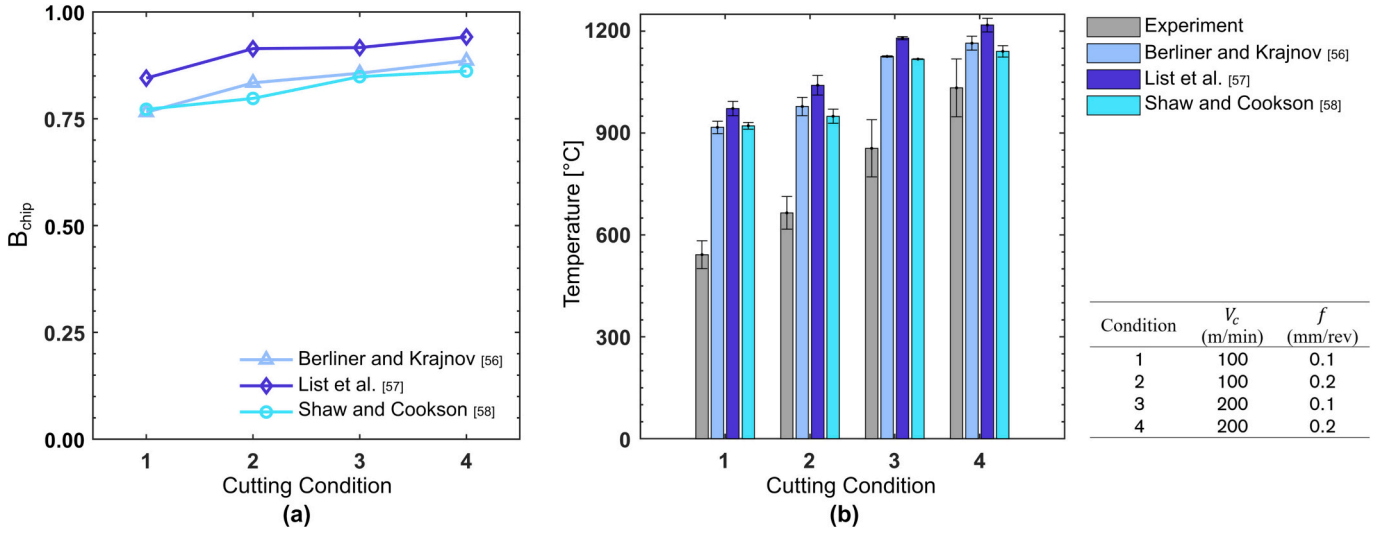

Condition	V_c (m/min)	f (mm/rev)
1	100	0.1
2	100	0.2
3	200	0.1
4	200	0.2

Fig. 11. (a) Comparison of the heat partition fractions evaluated using the three different formulae for the four cutting conditions of C45 steel and (b) the comparison of the experimental temperature measurements with the results using the different heat partition equations in Model II (V). The experimental data is taken from [41].

percentages using Model II (C) are 40 %, 48 % and 38 % using the Berliner and Krajnov, List et al., and Shaw and Cookson equations, respectively. The equation that leads to the lowest average error, albeit still fairly high, is the one by Shaw and Cookson; thus, it was selected for calculating B_{chip} in Models II (C) and (V) and reported in Table 4.

As is evident in Table 5, the increase in cutting speed from 100 to 200 m/min for the same feed led to an increase in the maximum temperature at the tool-chip interface. Upon increasing the speed for a constant feed of 0.1 mm/rev, the percentage increase in maximum chip temperature $T_{C,max}$ was 31 %, 41 %, 16 % and 25 % for Models I (C), I (V), II (C) and II (V), respectively. Similarly, for a constant feed of 0.2 mm/rev, the percentage increase was 36 %, 27 %, 23 % and 20 % for Models I (C), I (V), II (C) and II (V), respectively. Likewise, an increase in the feed for a constant cutting speed led to an increase in the maximum temperature, as expected. In addition, the agreement in maximum temperature between the chip side and the tool side for Models I (C) and

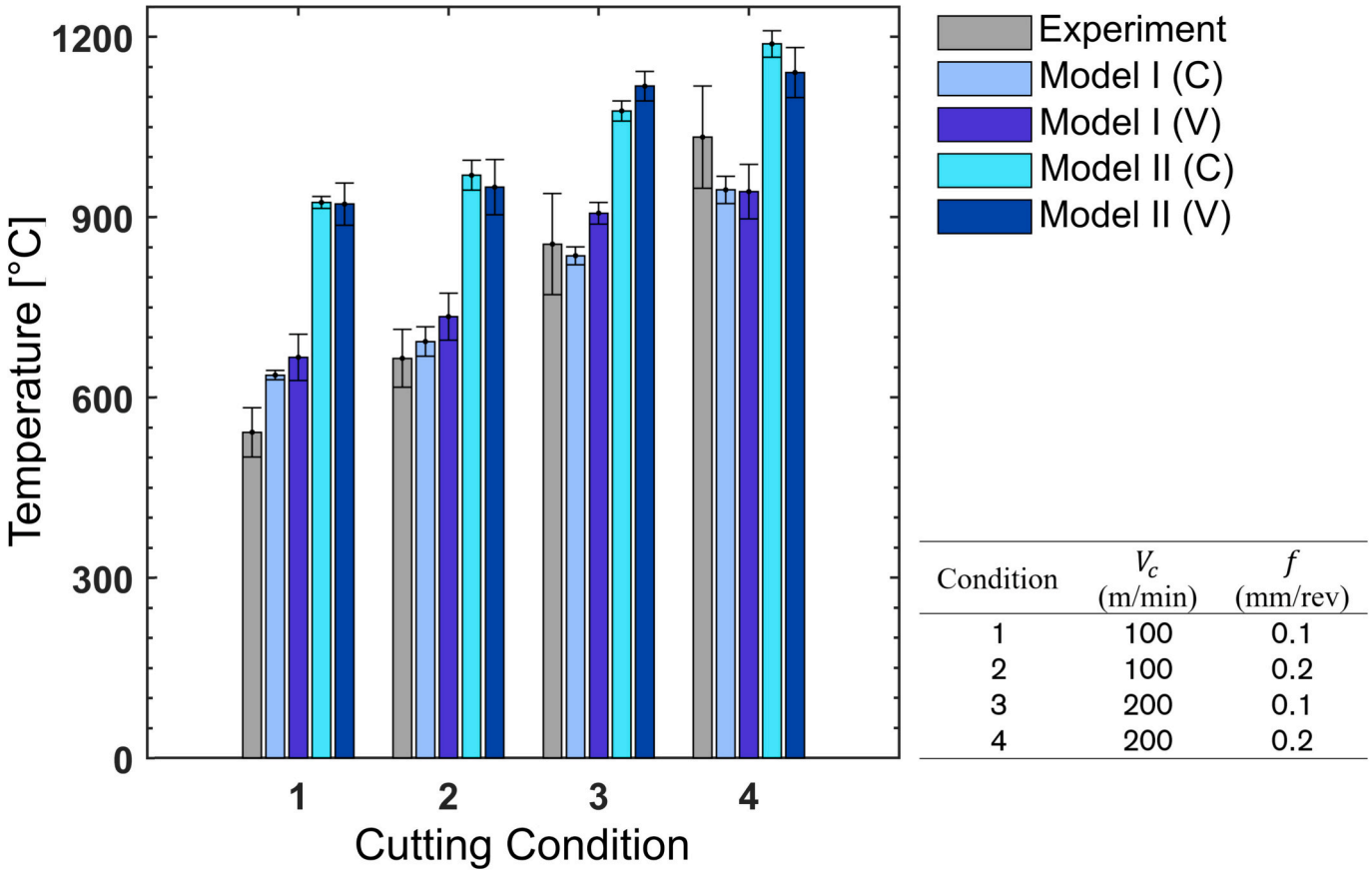

Condition	V_c (m/min)	f (mm/rev)
1	100	0.1
2	100	0.2
3	200	0.1
4	200	0.2

Fig. 12. Comparison of the experimental temperature measurements with the maximum interface temperature obtained from the different models for an ideal cutting edge for C45 steel. The experimental data is taken from [41].

(V) is evident, with the maximum difference between the two being 8°C for cutting condition 3 in Model I (C). This agreement between $T_{C,max}$ and $T_{T,max}$ indicates that the developed ML-based approach to determine the model parameters is reliable and leads to an accurate estimation of the heat partition coefficient (B_{chip}) in Model I. This is further supported by the obtained values of B_{chip} in Models I (C) and (V), where an increase in cutting speed and feed led to the expected increase in the heat partition in the chip [54]. In Model II, increasing the cutting speed for a constant feed also caused a decrease in the value of $\bar{T}_{PSZ}$, in line with the trends reported in the literature [26,41].

Similar observations are made in Table 6 for the orthogonal cutting of C50 using an ideal edge, where an increase in cutting speed from 100 m/min to 300 m/min led to an increase in the maximum chip temperature values by 45 %, 67 %, 36 % and 43 % for Models I (C), I (V), II (C) and II (V), respectively. The agreement between the maximum chip and tool temperatures is again evident, with the maximum difference between the two being 24°C for the case of cutting condition 1 in Model I (C). In addition, the heat partition coefficient B_{chip} increases with an increase in cutting speed, while $\bar{T}_{PSZ}$ decreases.

In order to assess each model's ability to estimate the maximum temperature, the temperature estimations were compared to the measurements reported when machining C45 steel under the same conditions. Fig. 12 summarises the prediction results and corresponding experimental measurements. It is evident that Model I (C) and Model I (V) exhibit better accuracy in predicting the maximum temperatures. The maximum error obtained using Model I (C) is 17 % for cutting condition 1, while it is 18 % for Model I (V) under the same cutting condition. Models II (C) and (V) exhibit a maximum error of 70 % and 63 %, respectively, both for cutting condition 1. This indicates that with an ideal cutting-edge assumption, Models I (C) and (V) are capable of accurately predicting the value of the maximum temperature, noting that the modification to the model did not significantly affect the value of the maximum temperature obtained. The maximum deviation between Models I (C) and (V) comes from cutting condition 3, where the temperature obtained by Model I (V) is 7 % higher than that of Model I (C).

The discrepancy in the temperature estimations stems from the underlying assumptions, for example, the model parameters. The impact of some of the key parameters in the modified models – Model I (V) and Model II (V) – is discussed in Section 5.3. In addition, within the context of Model II, the overestimation of the maximum interface temperature owes, to a great extent, to the choice of heat partition coefficient. The estimated heat partitioning coefficient using Shaw and Cookson, despite being the best estimation among the explored heat partitioning equations, is still significantly larger than those obtained using the ML-based algorithm in Model I (C) and Model I (V) under all cutting conditions (see Tables 5 and 6). This is believed to be the major reason for overestimation of the interface temperature in Model II, for which the absence of the mating tool surface precludes the in-process assessment of the heat partitioning coefficient.

Fig. 13 shows the temperature distribution inside the chip and tool for all cutting conditions of C45 steel using each of the implemented semi-analytical models. As discussed, the values of the maximum temperatures in Models I (C) and Model I (V) are lower than those obtained by Models II (C) and (V), which is evident in the plots of Fig. 13. While the maximum temperatures do not differ considerably between the original and enhanced models, the inclusion of a variable heat flux significantly affects the location of the maximum temperature. While both original models, i.e., Models I (C) and II (C), show a maximum temperature near the end of the contact length, the variable heat flux along the tool-chip interface shifts the location of this maximum temperature closer to the cutting edge in the case of both enhanced models –

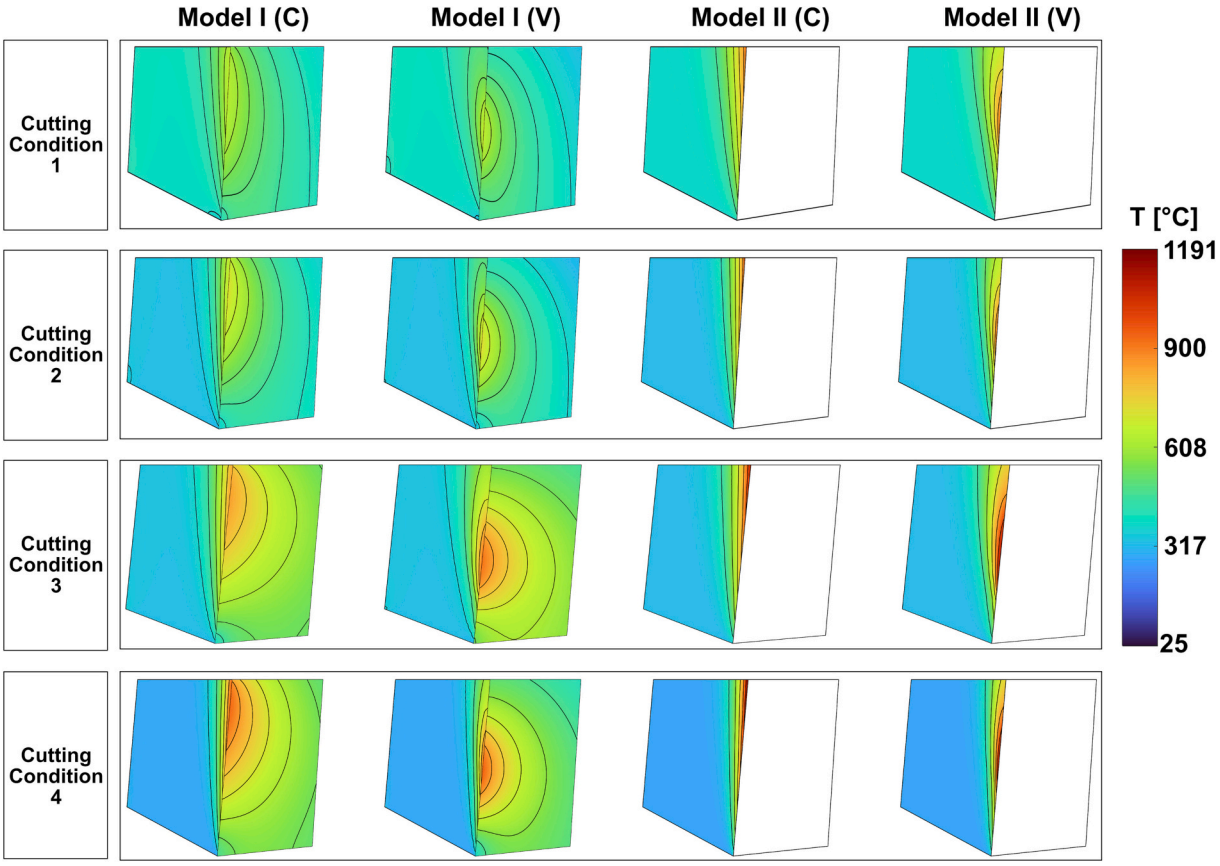

Fig. 13. Chip and tool temperature profiles obtained from the different semi-analytical models for the different cutting conditions of C45 steel using an ideal cutting edge.

Models I (V) and II (V). This is an expected effect of the variable heat flux given that the maximum heat flux lies at the end of the transition region, where both the plastic deformation from the sticking zone and the frictional heat from the sliding zone are superposed to maximise the heat flux in that region, as discussed in Section 3.3 and demonstrated in Fig. 6.

In order to evaluate each model's capability in predicting the location of the maximum temperature, the crater wear profiles are assessed for each of the cutting conditions of C50 steel, where the maximum crater depth *KT* as well as its location *KM* are presented in Table 3. Evidently, the crater depth *KT* is significantly higher at a higher cutting speed for the same spiral cutting length, where the tool used at a cutting speed of 300 m/min exhibits a crater depth *KT* almost ten times deeper than the tool at 100 m/min. Since crater wear is a thermally accelerated wear mechanism, it is expected that the crater wear will reach its maximum depth around the same location as the maximum temperature [63]. Therefore, the location of the maximum crater depth *KM*, as defined in Section 2, can be used as a reference to determine the model's accuracy in predicting the location of the maximum temperature along the tool-chip interface. A comparison between the location of the maximum crater depth (*KM*) and the obtained interface temperature from the different models is presented in Fig. 14 for the cutting conditions of C50 steel. Evidently, the models that include a variable heat flux show a clear correspondence between the location of maximum temperature and the maximum crater depth. In contrast, the simulations using a constant heat flux exhibit a maximum temperature towards the end of their contact length, which does not reflect the actual tribological conditions at the tool-chip interface.

Fig. 15 shows a comparison between the location of the maximum crater wear (*KM*) and the location of the maximum temperature obtained by each model for the cutting conditions of C50 steel. It is evident that the enhanced models; Models I (V) and II (V), lead to a better estimation of the location of the maximum temperature, with the maximum error percentages obtained for Models I (C), I (V), II (C) and II (V) being 212 %, 24 %, 246 % and 39 % respectively. Models I (V) and II (V) also exhibit a much lower average percentage error across all cutting conditions, with their average errors being 8 % and 22 % respectively. Models I (C) and II (C), on the other hand, have an average error percentage of 169 % and 197 %, respectively.

As discussed in Section 3.3, the heat flux reaches a maximum value around the end of the transition zones of the contact length, thus causing the location of the maximum temperature to shift closer towards the cutting edge, as is evident in Fig. 15. The length of the region along the contact length encompassing the sticking and transition zones ($l_{st}+ l_{tr}$) shows a clear correlation with the location of the maximum temperature, with both varying in a proportional manner between the different cutting conditions. Evidently, the location of the maximum temperature was approximately double the length ($l_{st}+ l_{tr}$) for all cutting conditions in Model I (V).

In summary, when using an ideal cutting-edge assumption, the enhanced Model I (V) shows good predictability for both the maximum interface temperature as well as its location. On the other hand, Model II (V) predicts the location of the maximum temperature quite accurately but leads to an overshoot in the value of the maximum temperature itself. This suggests that Model I (V) can be used to predict the temperature profiles with good accuracy, while Model II (V) is capable of an accurate prediction subject to a more exact estimation of the heat partition.

5.2. Round cutting edge

The main findings of each model for C45 steel using a rounded

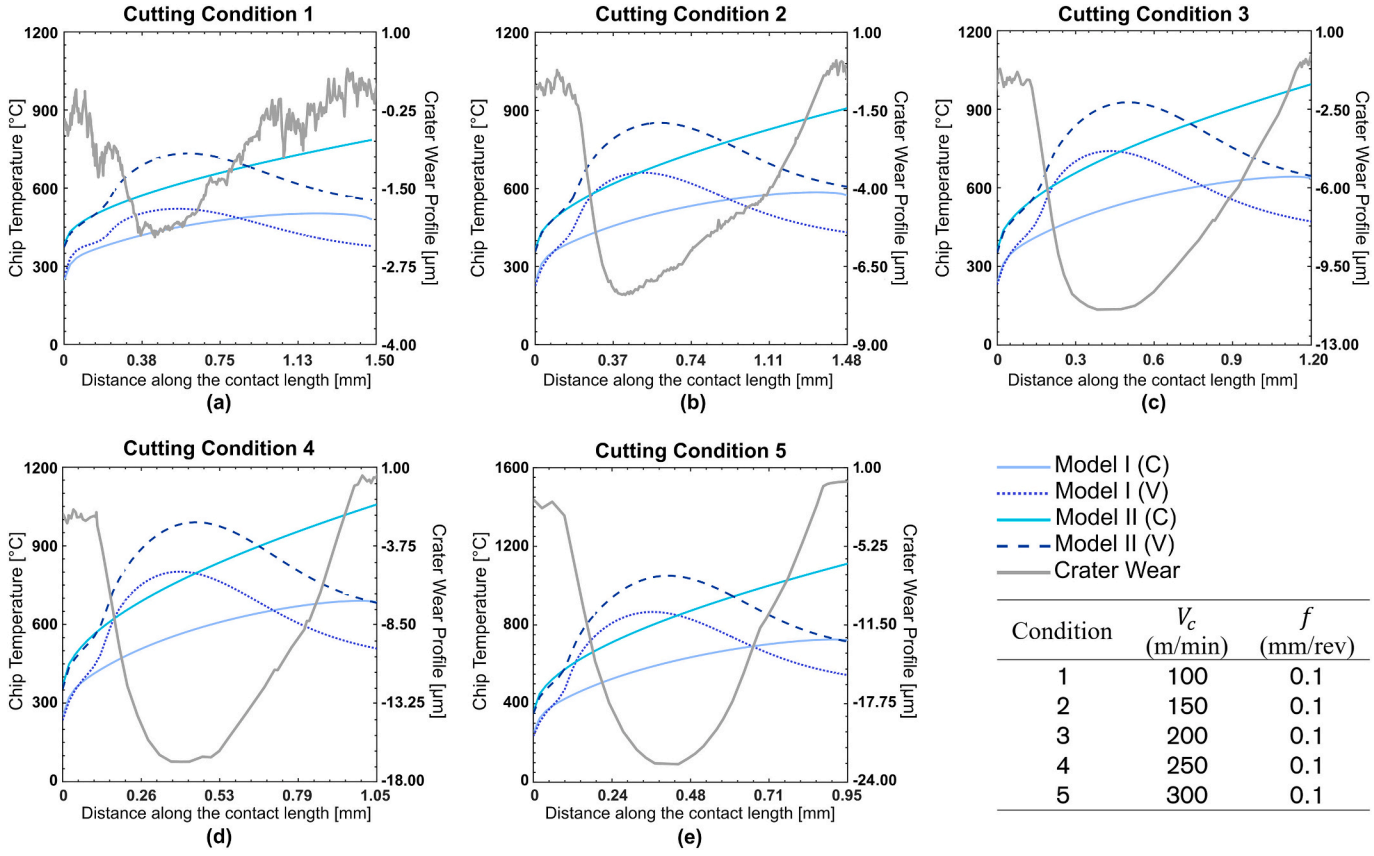

Condition	V_c (m/min)	f (mm/rev)
1	100	0.1
2	150	0.1
3	200	0.1
4	250	0.1
5	300	0.1

Fig. 14. The crater wear profiles measured when machining C50 at various cutting speeds and the interface temperature profiles obtained based on an ideal cutting-edge assumption (a–e).

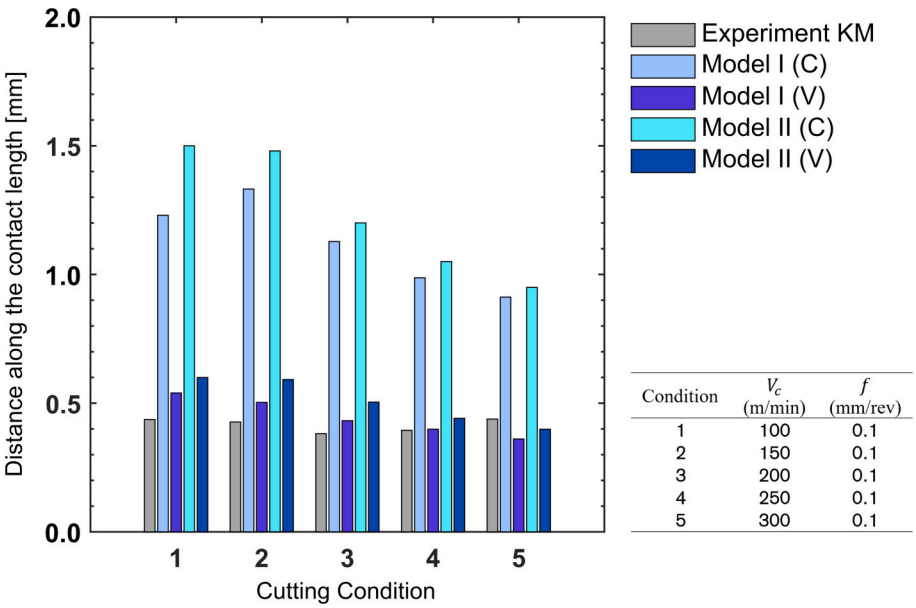

Condition	V_c (m/min)	f (mm/rev)
1	100	0.1
2	150	0.1
3	200	0.1
4	250	0.1
5	300	0.1

Fig. 15. Comparison of the location of maximum crater wear *KM* with the location of the maximum temperature for the cutting conditions of C50 steel using an ideal cutting edge.

Table 7
Main findings of the different models for all cutting conditions of C45 steel using a rounded cutting edge.

Model	Cutting condition	ϕ (°)	l_p (mm)	l_{st} [a] (mm)	l_{tr} [b] (mm)	σ_0 (MPa)	k_{SSZ} (Mpa)	$T_{C,max}$ (°C)	$T_{T,max}$ (°C)	B_{chip} (–)	$\bar{T}_{PSZ}$ (°C)
Model I (C)	1	15.7 ± 0.4	0.05	–	–	1737 ± 186	478 ± 31	461 ± 11	476 ± 13	0.50	–
	2	20.4 ± 0.2	0.05	–	–	1786 ± 130	450 ± 10	561 ± 12	542 ± 9	0.55	–
	3	19.9 ± 1.0	0.05	–	–	1326 ± 42	402 ± 15	635 ± 4	645 ± 1	0.74	–
	4	24.8 ± 0.7	0.05	–	–	1729 ± 50	342 ± 8	732 ± 8	733 ± 9	0.77	–
Model I (V)	1	15.7 ± 0.4	0.05	0.118	0.059	1739 ± 188	478 ± 31	373 ± 41	370 ± 36	0.50	–
	2	20.4 ± 0.2	0.05	0.243	0.122	1787 ± 130	451 ± 9	489 ± 35	488 ± 35	0.56	–
	3	19.9 ± 1.0	0.05	0.118	0.059	1327 ± 41	402 ± 15	531 ± 14	544 ± 14	0.57	–
	4	24.8 ± 0.7	0.05	0.243	0.122	1728 ± 49	342 ± 7	558 ± 25	562 ± 25	0.63	–
Model II (C)	1	15.7 ± 0.4	0.05	–	–	1737 ± 186	479 ± 31	695 ± 22	–	0.76	335 ± 13
	2	20.4 ± 0.2	0.05	–	–	1786 ± 131	451 ± 10	799 ± 19	–	0.79	307 ± 7
	3	19.9 ± 1.0	0.05	–	–	1326 ± 42	401 ± 15	844 ± 7	–	0.83	322 ± 7
	4	24.8 ± 0.7	0.05	–	–	1729 ± 50	342 ± 7	930 ± 14	–	0.86	284 ± 9
Model II (V)	1	15.7 ± 0.4	0.05	0.118	0.059	1737 ± 186	479 ± 31	571 ± 50	–	0.76	334 ± 13
	2	20.4 ± 0.2	0.05	0.243	0.122	1787 ± 130	450 ± 10	677 ± 41	–	0.79	307 ± 7
	3	19.9 ± 1.0	0.05	0.118	0.059	1326 ± 42	402 ± 15	714 ± 21	–	0.84	322 ± 7
	4	24.8 ± 0.7	0.05	0.243	0.122	1729 ± 49	341 ± 8	732 ± 34	–	0.86	285 ± 9

[a] $l_{st} = 1.25f$
[b] $l_{tr} = 0.5l_{st}$

cutting-edge tool are summarised in Table 7. Similar to the ideal cutting-edge case, l_{st} was estimated to be 25 % greater than the feed, and the transition length l_{tr} was then estimated to be half of l_{st}. The values of B_{chip} reported for Models II (C) and (V) correspond to the values obtained using the Shaw and Cookson equation. For Models I (C) and (V), the value of B_{chip} was obtained using the ML-based optimisation algorithm, discussed in Section 4.1, which led to the optimal match between the temperatures on the chip and tool sides.

Table 7 shows similar trends as in the case of an ideal cutting edge, where the increase in cutting speed for the same feed led to an increase in the maximum temperature at the tool-chip interface. For a constant feed of 0.1 mm/rev, the increase in speed from 100 to 200 m/min led to an increase in maximum chip temperature $T_{C,max}$ by 40 %, 45 %, 22 % and 26 % for Models I (C), I (V), II (C) and II (V), respectively. Similarly, for a feed of 0.2 mm/rev, the percentage increases were 32 %, 15 %, 17 % and 8 % for the four models, respectively. An increase in the feed for a constant cutting speed also led to an expected increase in the maximum temperatures $T_{C,max}$, where increasing the feed from 0.1 to 0.2 mm/rev for a cutting speed of 100 m/min led to a percentage increase of 23 %, 33 %, 16 % and 19 % for Models I (C), I (V), II (C) and II (V), respectively. For the cutting speed of 200 m/min, the increases were less prominent, with the percentages being 16 %, 5 %, 10 % and 2 % for the four models. For Models I (C) and (V), which utilise the ML-based approach to determine the optimal model parameters, the agreement between the tool and chip maximum temperatures is evident, with the maximum discrepancy between the two being 19°C for Model I (C) and 13°C for Model I (V). The resulting values of B_{chip} in Models I (C) and (V) then follow the expected trend, where an increase in cutting speed and feed yields a higher value of the chip heat partition. Similarly, using Shaw and Cookson to calculate the value of B_{chip} in Models II (C) and (V)

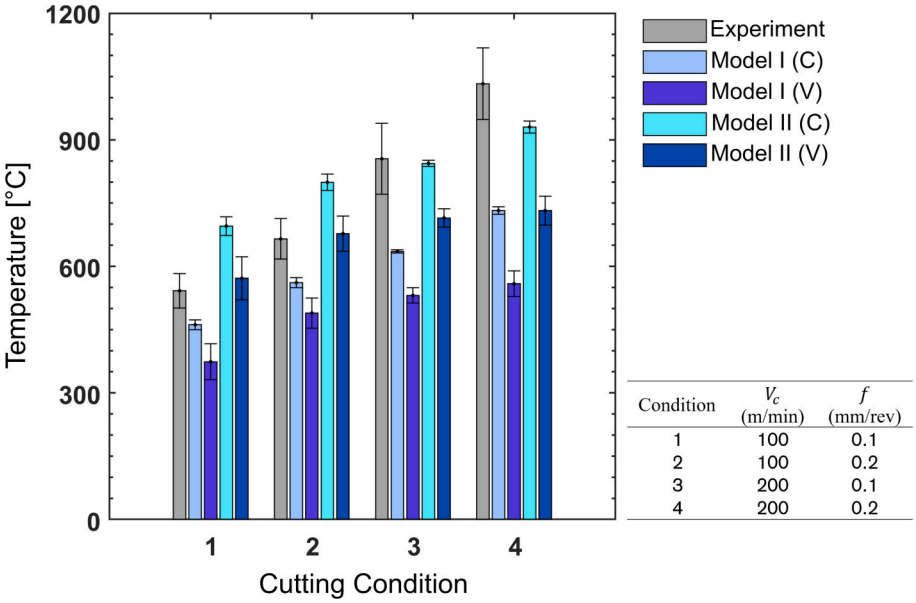

Fig. 16. Comparison of the experimental temperature measurements with the maximum interface temperature obtained from the different models for a round cutting edge for C45 steel. The experimental data are taken from [41].

yields increasing values of B_{chip} for an increase in cutting speed and feed.

Fig. 16 shows a comparison between the experimental temperature measurements and the estimated temperatures using the four models with a round cutting-edge assumption. It is evident then that Models II (C) and (V) lead to improved accuracy compared to Models I (C) and (V). The maximum percentage error for predicting the maximum temperature at the interface is then 32 %, 48 %, 24 % and 32 % for Models I (C), I (V), II (C) and II (V), respectively. The average error also shows that Models II (C) and (V) perform better with a round cutting-edge assumption, with the average error percentages being 25 %, 38 %, 14 % and 13 % for the four models, respectively.

For all the cutting conditions, all four models showed a significant decrease in the cutting temperatures when compared to the ideal cutting-edge assumption (cf. Fig. 12). On average for all cutting conditions, Models I (C), I (V), II (C) and II (V) led to a percentage decrease in maximum temperature of 26 %, 42 %, 24 % and 35 %, respectively. While the round cutting-edge geometry led to a significant decrease in the maximum temperature, the inclusion of a round edge did not significantly alter the location of the maximum temperature. The decrease in cutting temperatures for a rounded cutting edge is, to a large extent, associated with the exclusion of the heat source associated with the ploughing forces (see Section 3.2). The elimination of the ploughing force translates into a reduction in the normal and shear forces acting on the rake face and shear plane, and thus reduced heat generation at the primary and secondary shear zones, as shown in Table 8. When considering the tool with a round cutting edge, the normal force on the rake face (F_n) exhibited a decrease of 10 %, 5 %, 9 % and 5 % for cutting conditions 1, 2, 3 and 4, respectively, whereas the shear force (F_s) showed a more pronounced decrease with percentages of 23 %, 12 %, 14 % and 9 % for the different cutting conditions. Similarly, the friction force (F_f) exhibited a decrease of 27 %, 20 %, 24 % and 24 % when considering a round cutting-edge tool compared to an ideal tool. Subsequently, the heat intensity in the primary shear zone (q_{PSZ}) underwent a reduction of 23 %, 12 %, 14 % and 9 % for cutting conditions 1, 2, 3 and 4, which coincide well with the percentage drops observed for the shear force. In the secondary shear zone, for Models I (C) and II (C), which considered a constant heat flux, q_{SSZ} underwent a reduction of 37 %, 26 %, 35 % and 31 % for the respective cutting conditions. For the case of variable heat flux, as in Models I (V) and II (V), the maximum value of the heat flux ($q_{SSZ,max}$) also exhibited a decrease when switching from an ideal to a round cutting edge. The percentage decreases were respectively 58 %, 42 %, 52 % and 49 % for the different cutting conditions. These decreases in cutting forces and heat intensities led to the clear drop in estimated temperatures at the interface. While for Models II (C) and (V), this worked as a counterbalance to the overestimation of the heat partition coefficient and thus led to a better estimation of the temperatures, for Models I (C) and (V), this led to a significant underestimation of the maximum temperature and increased their average error percentages markedly. Despite being practised in several studies [25,35], it is important to emphasise here that neither Model I nor Model II can, in principle, account for the heat source due to ploughing force (i.e., heat generation in the ternary shear zone). Hence, exclusion of its

Table 8
Comparison between the main findings of an ideal versus round cutting edge for C45 steel.

Tool geometry	Cutting condition	F_f (N)	F_n (N)	F_s (N)	q_{PSZ} (10^2 J/mm^{2}s)	q_{SSZ} (10^2 J/mm^{2}s)	$q_{SZZ,max}$ (10^2 J/mm^{2}s)
Ideal	1	471 ± 24	521 ± 7	405 ± 7	8.41 ± 0.10	2.33 ± 0.33	4.27 ± 0.28
	2	657 ± 30	884 ± 17	655 ± 11	8.46 ± 0.04	2.09 ± 0.15	3.78 ± 0.77
	3	413 ± 14	482 ± 5	333 ± 13	18.00 ± 0.38	4.10 ± 0.32	8.46 ± 0.52
	4	522 ± 17	811 ± 20	559 ± 23	18.03 ± 0.15	4.41 ± 0.28	7.67 ± 0.15
Round	1	341 ± 38	470 ± 5	310 ± 15	6.45 ± 0.11	1.47 ± 0.11	1.82 ± 0.17
	2	524 ± 40	835 ± 16	578 ± 16	7.48 ± 0.12	1.55 ± 0.06	2.19 ± 0.13
	3	315 ± 17	441 ± 4	285 ± 9	15.42 ± 0.41	2.69 ± 0.14	4.08 ± 0.02
	4	395 ± 22	774 ± 19	509 ± 21	16.44 ± 0.14	3.06 ± 0.13	3.92 ± 0.12

contribution from the normal and shear forces acting on the rake face without accounting for heat generation due to ternary deformation can lead to significant underestimation. Evidently, the deviation from the experimental measurements depends on the choice of stagnation angle as it dictates the intensity of heat flux on the shear plane and the rake face (see Section 5.3).

5.3. Impact of key model parameters

Given that the models discussed in this work rely on the values of different model parameters to calculate the stress and temperature distributions, as discussed in the previous sections, it is important to determine the sensitivity of the models to those parameters. Here, a sensitivity analysis is conducted using Model II (V) for C50 steel using both an ideal and a round-edged cutting tool. The sensitivity analysis is performed using a central composite design, varying two factors at a time for each cutting-edge geometry. The simulation results were then used to build a multilinear quadratic model by regression analysis.

In the case of an ideal cutting-edge geometry, the roles of the exponential constant ξ used in the normal stress distribution along the rake face (Eq. (13)) and the shear stress distribution constant n (Eq. (14)) were investigated. Here, the exponential constant ξ for the stress distribution along the ploughing length l_p was kept constant ($\xi = 3$). The effect of these parameters on the maximum temperature and its location (i.e., distance from the cutting edge) is shown in Fig. 17. It should be noted that the selection of these parameters was based on the results of a preliminary analysis to determine the most impactful model parameters. For example, the preliminary analysis suggested that the Taylor-Quinney coefficient η (Eqs. (2) and (3)) only affects the amplitude of the temperature, while the thickness of the secondary shear zone δ (Eqs. (15) and (18)) does not exhibit a significant effect on either the maximum temperature or its location.

Fig. 17a shows the clear dependence of the maximum temperature on the value of the shear stress constant n, where increasing the value of n seems to have opposite effects on the maximum temperature, depending on which range its value lies in. For instance, a variation of n between 1.0×10^{-3} and approximately 4.5×10^{-3} shows that an increase in n leads to a decrease in maximum temperature. In contrast, varying n in the range of 4.5×10^{-3} to 7.0×10^{-3} exhibits the opposite effect. In fact, a lower value of n yields a higher maximum shear stress (k_{SSZ}) and thus is expected to yield a higher maximum heat flux (based on the force-balance equations in Appendix I). A lower value of n also dictates a steeper decrease of the shear stress distribution along the contact length, while the interface velocity ($V_{\chi,\psi}$) is independent of n. This can lead to opposing behaviours, as the resulting heat flux depends on the product of the shear stress (τ) and velocity ($V_{\chi,\psi}$) along the tool-chip interface (see Eq. (15)). For example, if the amplitude of the shear stress is high enough to partly compensate for the impact of its sharp decrease, then a lower value of n will lead to a higher temperature, as seen between 1.0×10^{-3} and 4.5×10^{-3}. However, if the decay of the shear stress along the tool-chip interface is slow enough to compensate for its lower maximum value, then a higher n can lead to a higher maximum temperature, as seen in the range of 4.5×10^{-3} to 7.0×10^{-3}. As also shown in Fig. 17a, increasing ξ for a constant n seems to consistently lead to an increase in the maximum temperature. For instance, for a constant n value of 4.5×10^{-3}, increasing ξ from 1.50 to 4.50 increases the maximum temperature by 8 %. This is due to the effect that ξ has on the normal stress (σ) and subsequently the shear stress (τ) distribution. A higher ξ leads to a higher σ_0 and k_{SSZ}, which consequently leads to an increase in the heat flux distribution along the tool-chip interface.

Fig. 17b shows an evident dependence of the location of the maximum temperature on both stress exponential constants, ξ and n. For instance, for a fixed value for $n = 4.5 \times 10^{-3}$, as used in this work, increasing ξ from 1.50 to 4.50 causes the location of the maximum temperature to decrease from 0.64 mm to 0.42 mm, indicating a 34 % decrease. In contrast, for a fixed value of ξ=3.0, increasing n from 1×10^{-3} to 7×10^{-3} causes the location of the maximum temperature to increase by 48 % from 0.35 mm to 0.52 mm. These exponential constants have such an important effect on the location of the maximum temperature since they directly influence the location of maximum normal and shear stress along the contact length, as mentioned previously. An increase in the value of n causes the location of the maximum heat flux to shift further away from the cutting edge, whereas a higher value of ξ exhibits the opposite effect.

For a round-edged cutting tool, the sensitivity analysis was performed to assess the effect of the stagnation angle θ_S (see Appendix I) and the sum of the sticking and transition lengths ($l_{st} + l_{tr}$) (Eqs. (15) and (17)) on both the maximum temperature and its location. The results of this sensitivity analysis are depicted in the plots of Fig. 18.

Fig. 18a shows the sensitivity of the maximum temperature to the value of θ_S and the sum of the sticking and transition lengths ($l_{st} + l_{tr}$). It is clear that the maximum temperature is affected by the stagnation

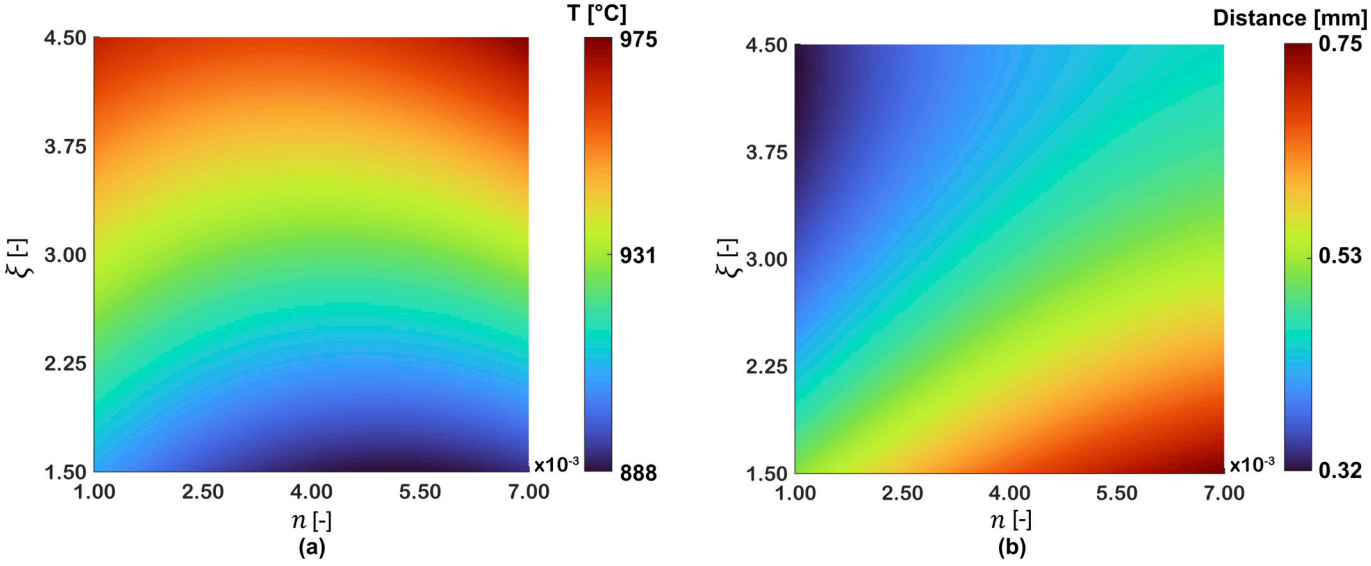

Fig. 17. Variation of (a) the maximum temperature and (b) its location with respect to the normal stress exponential constant ξ and the shear stress exponential constant n with an ideal cutting-edge geometry for the case of C50 steel ($V_c = 200$ m/min and $f = 0.1$ mm/rev).

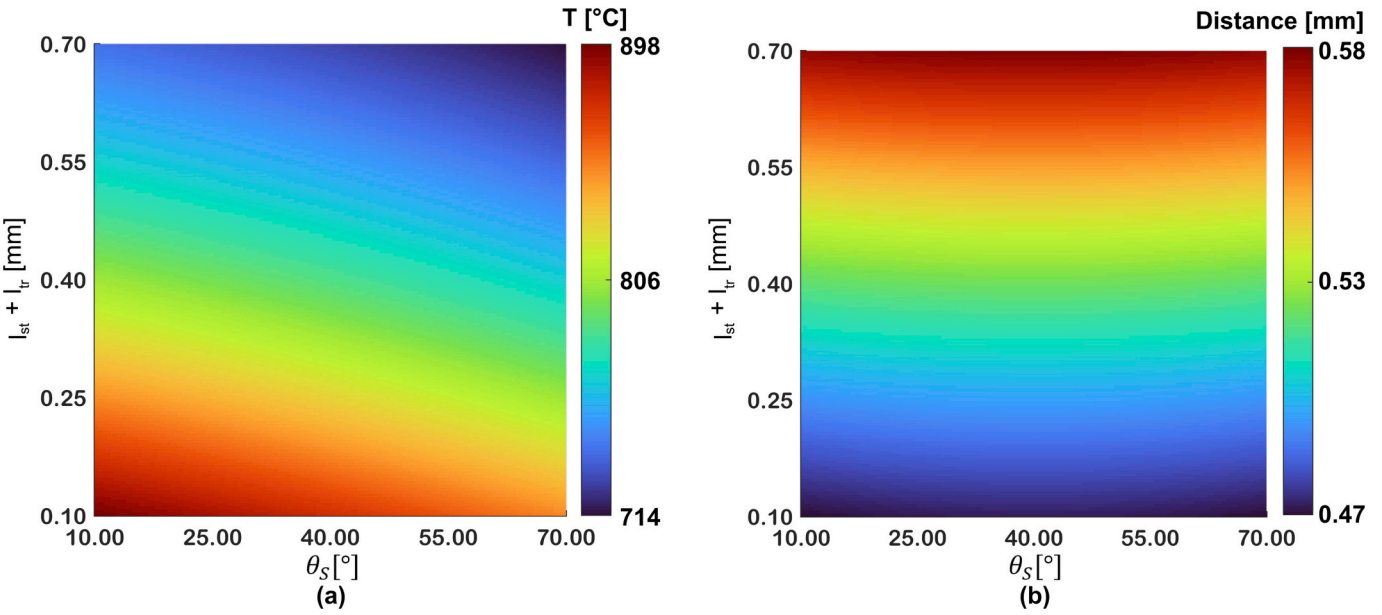

Fig. 18. Variation of (a) the maximum temperature and (b) its location with respect to the stagnation angle θ_s and the sum of the sticking and transition lengths ($l_{st} + l_{tr}$) with a round cutting-edge geometry for the case of C50 steel ($V_C = 200$ m/min and $f = 0.1$ mm/rev).

angle θ_S, where its variation from 10° to 70° for a fixed $l_{st} + l_{tr}$=0.10 mm decreases the maximum temperature by 8 % from 898 °C to 830°C. This variation is due to the direct effect that the stagnation angle has on the normal and shear forces of the rake face and shear plane after considering the ploughing effect (see Appendix I). An increase in the stagnation angle leads to an increase in the ploughing depth h_p and thereby a decrease in the actual uncut chip thickness h_u. Consequently, both the shear angle ϕ and chip velocity V_{ch} undergo a decrease, leading to a decrease in the velocity distribution at the tool-chip interface ($V_{\chi,\psi}$). In addition, an increase in θ_S also leads to an increase in the ploughing length l_p, which decreases the normal and shear forces (i.e., F_n, F_f and F_s), leading to a reduction in the normal and shear stresses acting on the tool. As a result of both these effects, the heat flux in the secondary shear zone decreases (see Eq. (15)), leading to a reduction in the maximum temperature, as observed in Fig. 18a. In contrast, the stagnation angle has a less prominent effect on the location of the maximum temperature, as shown in Fig. 18b, where its variation from 10° to 70° for a fixed $l_{st} + l_{tr}$=0.10 mm shifts the location of the maximum temperature by <1 %. In fact, the stagnation angle has a negligible effect on the normal and shear stress distribution profiles, predominantly affecting the chip velocity V_{ch} amplitude and thus leading to a change in the amplitude of the resulting heat flux but not its location.

In addition, for the same value of $\theta_S = 40°$, a variation of the sum ($l_{st} + l_{tr}$) from 0.10 to 0.70 mm shows a decrease of 17 % in maximum temperature, indicating that the maximum temperature is more sensitive to this sum than to the stagnation angle. This is because the sticking (l_{st}) and transition (l_{tr}) lengths have a direct effect on the value of the non-dimensional local coordinates χ, ψ and κ (Eqs. (17a)–(17c)) used to calculate the velocity distribution at the tool-chip interface ($V_{\chi,\psi}$) as well as the shear strain rate $\dot{\gamma}$ (see Appendix II). Since longer sticking and transition lengths indicate that the velocity distribution reaches its maximum value further along the contact length, this means that the maximum velocity coincides with lower shear stress, leading to a lower maximum value of their product and subsequently a lower maximum of the heat flux (see Eq. (15) and Fig. 5). This justifies the lower temperature obtained for a larger sum of ($l_{st} + l_{tr}$). In addition, the sum of ($l_{st} + l_{tr}$) shows a notable effect on the location of the maximum temperature, as observed in Fig. 18b, where for instance, increasing the sum from 0.10 to 0.70 mm at a fixed value of $\theta_S = 40°$ shifted the location of the maximum temperature 17 % further away from the cutting edge. An increase in the sum of ($l_{st} + l_{tr}$) implies that the sliding region has also shifted further away from the cutting edge. Given that the maximum temperature coincides with the point where the summed contribution of the sticking and sliding heat fluxes is at its maximum, it is therefore reasonable that the location of the maximum temperature shifts away from the cutting edge.

The sensitivity of the maximum temperature and its location to the exponential constants, stagnation angle and sum of ($l_{st} + l_{tr}$) emphasises the importance of selecting suitable model parameters to yield accurate results. While literature includes different models to calculate, for example, the sticking and sliding contact lengths and distribution of shear and normal stresses [49], it would be more accurate to rely on the measured values where applicable. For uncoated tools, in particular, the length of the sticking zone and the total contact length can be estimated well using an appropriate optical profilometer or by an SEM (see Fig. 19a–b). While the WC grains in the sliding region (zone 2) are smoothly polished, their surface is relatively much rougher in zone 3 (sticking zone) and resembles the topography of unworn surfaces outside the contact area (zone 1). This distinction in topography of WC grains suggests that the sliding velocity approaches zero on the tool surface in the sticking region near the cutting edge, while the chip continually slides on the rake face in the sliding zone (zone 3), resulting in a smooth surface topography (see Fig. 19c). Similarly, the ploughing length on the flank surfaces can be measured using a microscope [40], allowing for a better estimation of the ploughing force of rounded cutting edges.

Nevertheless, developing reliable self-consistent models that do not rely on a trial-and-error selection of model parameters or experimental measurements is still of great interest. A number of attempts have been made in this line of research, for example, the pioneering works of Oxley and his co-workers based on a modified slip-line theory [64–66]. However, most slip-line models still rely on an ideal cutting-edge assumption, which is inherently not an accurate representation of real cutting tools. On the other hand, those slip-line models that are extended for the round cutting edge [64,67,68], in most cases, do not fully account for the elastic recovery on the clearance side of the tool adjacent to

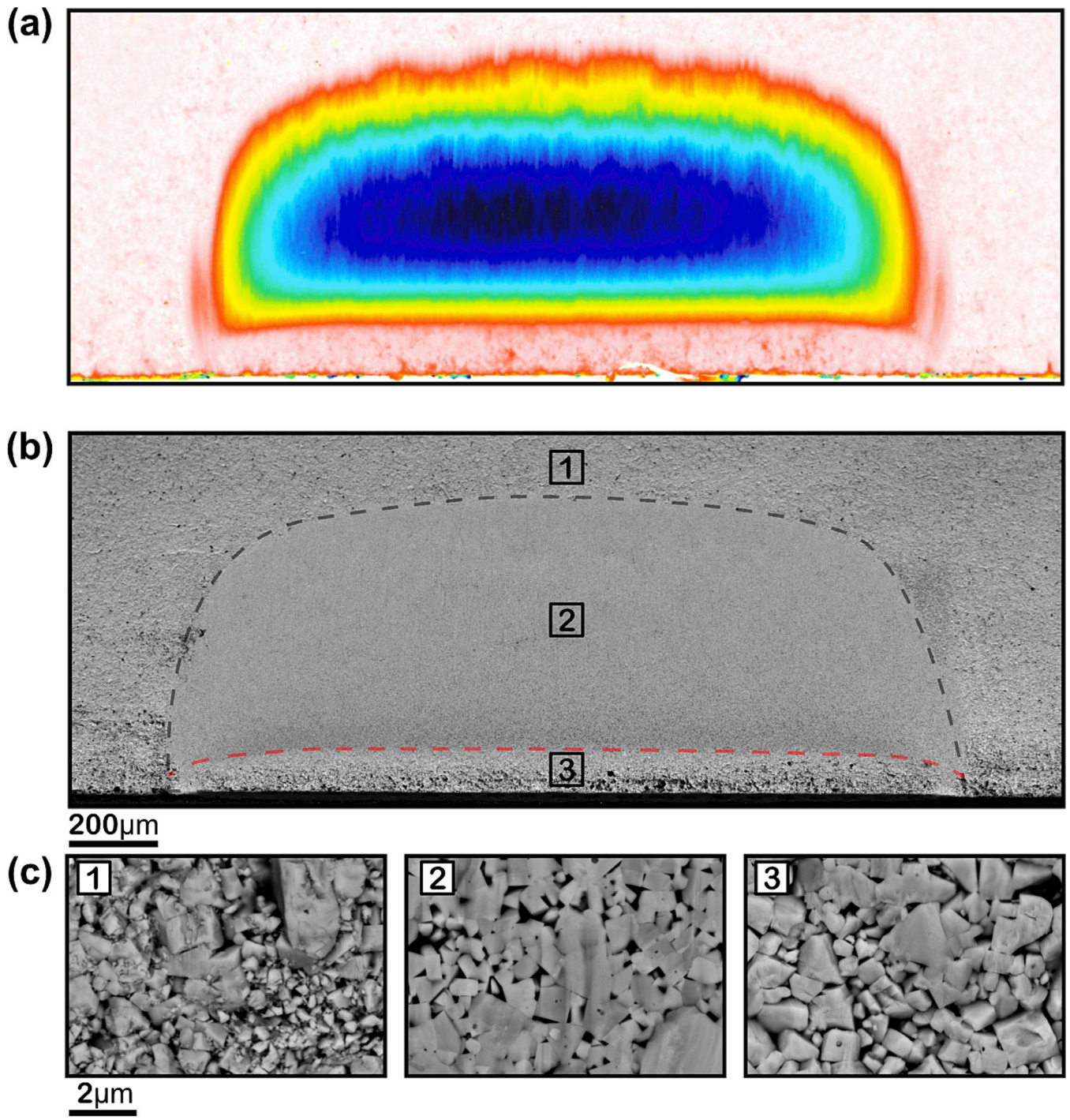

Fig. 19. (a) Examination of crater wear development using an optical profilometer indicating sticking and sliding zones on the tool's rake face when machining C50 steel at 300 m/min; (b) an overview of the worn surface analysed using the scanning electron microscope – the tool is tilted 21° for a better visualisation; and (c) the detailed analysis of the surface topography of tool's rake face in regions 1–3 shown in (b).

the edge (i.e., the ploughing length; see Fig. 4). This, perhaps, showcases a research area that needs to be investigated further in the scientific community.

While the current research incorporates some effects that a round-edged cutting tool has on the resulting temperature profile, specifically by accounting for the ploughing effect on the cutting forces and stress distributions, further development of these semi-analytical models should focus on including the effect of the heat source associated with the ploughing effect on the flank side and around the cutting edge to overcome the underestimation of the cutting temperature in their vicinity, as observed in Fig. 13 for models I (V) and II (V). This limitation can largely be overcome by integrating FEM with semi-analytical thermal models [34,69]. Nevertheless, the enhanced models presented in this study show significant improvement in determining the maximum temperature and especially its location as compared to the original models. While the presented enhanced models already yield fairly accurate results, it becomes clear from the conducted analyses that these models are very sensitive to certain parameters, and the accuracy of their results is highly dependent on the correct selection of their values.

6. Conclusions

In this study, an investigation is performed on the effect of incorporating a variable heat flux into two well-established semi-analytical temperature models. Based on an in-depth comparative analysis, the following conclusions can be drawn:

- Including a variable heat flux along the tool-chip interface has little effect on the value of the maximum interface temperature, but it significantly improves the accuracy in predicting its location. The modified Komanduri and Hou model, Model I (V), with a variable heat flux shows good accuracy in predicting both the maximum temperature (% maximum error) and its location (% maximum error). This is of vital importance for an accurate estimation of crater wear evolution during machining.
- Komanduri and Hou's model yields improved accuracy in predicting the maximum cutting temperature compared to the model presented by Moufki and his co-workers (Model II) incorporating a similar heat flux. This is largely attributed to the temperature pairing along the interface between the chip and tool in Komanduri and Hou's model as a part of the solution, allowing for determination of the variable heat partition. In contrast, the temperature estimations in Model II presented by Moufki and his co-workers require prior knowledge of the heat partitioning coefficient between the tool and chip, and thus the accuracy of temperature predictions depends to a large extent on the reliability of the adopted heat partitioning equations. Furthermore, the developed ML-based approach provides a promising framework to determine the heat partitioning parameters in Komanduri and Hou's model, allowing for more efficient and reliable temperature predictions.
- A detailed iterative approach was presented to obtain the ploughing force exerted on round cutting edges. The modelling of a round-edged cutting tool led to a significant decrease in the cutting temperature due to the exclusion of the heat source associated with the ploughing forces, as well as the decrease in the normal and shear forces acting on the tool's rake face.
- A parametric investigation using Model II with a variable heat source and an ideal cutting-edge showed a high dependence of the maximum temperature and its location on the normal stress exponential coefficient ξ and the shear stress exponential coefficient n. Similar investigations using a round cutting edge showed the dependence of the maximum temperature and its location on the stagnation angle θ_s and the sum of the sticking and transition lengths ($l_{st} + l_{tr}$).

Declaration of competing interest

The authors declare that they have no known competing financial interests or personal relationships that could have appeared to influence the work reported in this paper.

Acknowledgements

This study was part of the WEAR-FRAME project funded by Vinnova (Sweden's Innovation Agency) under the FFI programme (Project No. 2020-05179). The support received from the Chalmers Production Area of Advance and the Chalmers Centre for Metal Cutting Research (MCR) is also acknowledged.

Appendix I

The normal stress σ and shear stress τ distributions are given by the following relations, respectively, as presented in the manuscript in Eqs. (13) and (14):

$$\sigma = \sigma_0 \left(1 - \frac{y^{'}}{l_c}\right)^{\xi} \tag{A.1}$$

$$\tau = k_{ssz}(1 - e^{-n\sigma}) \tag{A.2}$$

The ploughing length l_p is obtained using the following relationship with reference to Fig. 4a:

$$l_p = r_e \left(\frac{cos\alpha - cos\theta_S}{sin\alpha}\right) \tag{A.3}$$

The projected components of normal and shear forces in the cutting and feed force directions are then given by the relations shown in Eqs. (A.4)–(A.7). With reference to Fig. 4a, the projected components of the normal forces in the cutting direction are calculated using the following equation:

$$F_N = \int_0^{l_c} \sigma w cos\gamma dy^{'} + \int_0^{\gamma} \sigma_0 w r_e cos\theta d\theta + \int_{\theta_S}^{\frac{\pi}{2}} \sigma_0 w r_e sin\theta d\theta + \int_0^{\theta_S} \sigma_0 w r_e sin\theta d\theta - \int_0^{\alpha} \sigma_0 w r_e sin\theta d\theta - \int_0^{l_p} \sigma w sin\alpha dx^{'} \tag{A.4}$$

A similar derivation leads to the following expression for the projected component of the shear force in the cutting direction:

$$F_T = \int_0^{l_c} \tau w sin\gamma dy^{'} + \int_0^{\gamma} k_{SSZ}(1 - e^{-n\sigma_0}) w r_e sin\theta d\theta - \int_{\theta_S}^{\frac{\pi}{2}} k_{SSZ}(1 - e^{-n\sigma_0}) w r_e cos\theta d\theta + \int_0^{\theta_S} k_{SSZ}(1 - e^{-n\sigma_0}) w r_e cos\theta d\theta + \int_0^{\alpha} k_{SSZ}(1 - e^{-n\sigma_0}) w r_e cos\theta d\theta + \int_0^{l_p} \tau w cos\alpha dx^{'} \tag{A.5}$$

Similarly, the expression for the projected components of the normal forces in the feed force direction is derived as:

$$F_N^{'} = -\int_0^{l_c} \sigma w sin\gamma dy^{'} - \int_0^{\gamma} \sigma_0 w r_e sin\theta d\theta + \int_{\theta_S}^{\frac{\pi}{2}} \sigma_0 w r_e cos\theta d\theta + \int_0^{\theta_S} \sigma_0 w r_e cos\theta d\theta + \int_0^{\alpha} \sigma_0 w r_e cos\theta d\theta + \int_0^{l_p} \sigma w cos\alpha dx^{'} \tag{A.6}$$

And the expression for the projected components of the shear forces projected in the feed force direction is derived as:

$$F_T^{'} = \int_0^{l_c} \tau w cos\gamma dy^{'} + \int_0^{\gamma} k_{SSZ}(1-e^{-n\sigma_0}) w r_e cos\theta d\theta + \int_{\theta_S}^{\frac{\pi}{2}} k_{SSZ}(1-e^{-n\sigma_0}) w r_e sin\theta d\theta - \int_0^{\theta_S} k_{SSZ}(1-e^{-n\sigma_0}) w r_e sin\theta d\theta + \int_0^{\alpha} k_{SSZ}(1-e^{-n\sigma_0}) w r_e sin\theta d\theta + \int_0^{l_p} \tau w sin\alpha dx^{'} \tag{A.7}$$

The cutting and feed force can then be calculated for given σ_0 and k_{SSZ} as:

$$F_{c,calc} = F_N + F_T \tag{A.8a}$$

$$F_{t,calc} = F_N^{'} + F_T^{'} \tag{A.8b}$$

The σ_0 and k_{SSZ} can then be identified by solving the following equations using an iterative approach. This is done by minimising the following objective function using an appropriate optimisation algorithm:

$$\mathscr{R}(\sigma_0, k_{SSZ}) = \frac{1}{2}\sqrt{\left(F_c - F_{c,calc}(\sigma_0, k_{SSZ})\right)^2 + \left(F_t - F_{t,calc}(\sigma_0, k_{SSZ})\right)^2} \tag{A.9}$$

where F_c and F_t are the measured cutting and feed force, respectively.

Appendix II

The shear strain γ_s at a given location within the SSZ can be obtained using the following equation, assuming the unidirectional material deformation in the sticking zone is perpendicular to the chip flow direction y (see Fig. 5a):

$$\gamma_s = \frac{du}{dx} \tag{B.1}$$

where u is the displacement in the y-direction within the SSZ. The shear strain rate $\dot{\gamma}$ at a given location within the SSZ can then be given by the following partial derivatives,

$$\dot{\gamma} = \frac{dV}{dx} = \frac{dV}{d\psi}\frac{d\psi}{dx} + \frac{dV}{d\chi}\frac{d\chi}{dx} \tag{B.2}$$

Since χ is only a function of y (see Eq. (17a)), the shear strain rate can be simplified to Eq. (B.3):

$$\dot{\gamma} = \frac{dV}{d\psi}\frac{d\psi}{dx} \tag{B.3}$$

Using $V_{\chi,\psi}$ from Eq. 16, the shear strain rate becomes

$$\dot{\gamma} = \frac{1}{4} V_{ch}(1-\chi)(\chi - \chi\psi + \psi)^{-\frac{3}{4}} \times \frac{1}{\delta(1-\kappa)} \tag{B.4}$$

$$\dot{\gamma} = \frac{1}{4} \frac{V_{ch}(1-\chi)}{\delta(1-\kappa)}(\chi - \chi\psi + \psi)^{-\frac{3}{4}} \tag{B.5}$$

Substituting $\chi - \chi\psi + \psi = \left(\frac{V_{\chi,\psi}}{V_{ch}}\right)^4$,

$$\dot{\gamma} = \frac{1}{4} \frac{V_{ch}(1-\chi)}{\delta(1-\kappa)} \left(\frac{V_{\chi,\psi}}{V_{ch}}\right)^{-3} \tag{B.6}$$

Knowing that $\kappa = \frac{y}{l_{st}+l_{tr}}$ (Eq. (19)) and $\chi = 0$ ($y < l_{st}$), the shear strain rate within the sticking zone may be further simplified as:

$$\dot{\gamma} = \frac{1}{4} \frac{V_{ch}(l_{st}+l_{tr})}{\delta(l_{st}+l_{tr}-y)} \left(\frac{V_{ch}}{V_{\chi,\psi}}\right)^3 \tag{B.7}$$

References

[1] Malakizadi A, Gruber H, Sadik I, Nyborg L. An FEM-based approach for tool wear estimation in machining. Wear 2016:10–24.

[2] Hoier P, Malakizadi A, Klement U, Krajnik P. Characterization of abrasion- and dissolution-induced tool wear in machining. Wear 2019;426-427:1548–62.

[3] Ning J, Liang SY. A comparative study of analytical thermal models to predict the orthogonal cutting temperature of AISI 1045 steel. The International Journal of Advanced Manufacturing Technology 2019;102:3109–19.

[4] Abukhshim NA, Mativenga PT, Sheikh MA. Heat generation and temperature prediction in metal cutting: a review and implications for high speed machining. International Journal of Machine Tools & Manufacture 2006;46:782–800.

[5] Grzesik W. Experimental investigation of the cutting temperature when turning with coated indexable inserts. Int J Mach Tool Manuf 1999;39(3):355–69.

[6] Komanduri R, Hou ZB. A review of the experimental techniques for the measurement of heat and temperatures generated in some manufacturing processes and tribology. Tribology International 2001;34:653–82.

[7] O'Sullivan D, Cotterell M. Temperature measurement in single point turning. J Mater Process Technol 2001;118:301–8.

[8] Zhao J, Liu Z, Wang B, Hu J, Wan Y. Tool coating effects on cutting temperature during metal cutting processes: comprehensive review and future research directions. Mechanical Systems and Signal Processing 2021;150.

[9] Tuğrul Ö, Taylan A. Process simulation using finite element method — prediction of cutting forces, tool stresses and temperatures in high-speed flat end milling. Int J Mach Tool Manuf 2000;40(5):713–38.

[10] Umbrello D, M'Saoubi R, Outeiro JC. The influence of Johnson–Cook material constants on finite element simulation of machining of AISI 316L steel. Int J Mach Tool Manuf 2007;47(3–4):462–70.

[11] Lazoglu CII, Altintas Y. A three-dimensional transient thermal model for machining. J Manuf Sci Eng 2016;138.

[12] Rosenthal D. The theory of moving sources of heat and its application to metal treatments. Transactions of ASME 1946;68:849–66.
[13] Jaeger J. Moving sources of heat and the temperature at sliding contacts. Proceedings of the Royal Society of New South Wales 1942;76:203–24.
[14] Blok H. Theoretical study of temperature rise at surfaces of actual contact under oiliness lubricating conditions. Proceedings of General Discussion on Lubrication and Lubricants, Institute of Mechanical Engineers London 1938;2:22–235.
[15] Hahn R. On the temperature developed at the shear plane in the metal cutting process. Journal of Applied Mechanics-Transactions of the ASME 1951;18(3).
[16] Trigger K, Chao B. An analytical evaluation of metal cutting temperature. Transactions of ASME 1951;73:57–68.
[17] Loewen E, Shaw M. On the analysis of cutting tool temperatures. Transactions of ASME 1954;71:217–31.
[18] Komanduri R, Hou ZB. Thermal modeling of the metal cutting process part I - temperature rise distribution due to shear plane heat source. International Journal of Mechanical Sciences 2000;42:1715–52.
[19] Wright PK, McCormick SP, Miller TR. Effect of rake face design on cutting tool temperature distributions. Journal of Engineering for Industry 1980;102:123–8.
[20] Moufki A, Molinari A, Dudzinski D. Modeling of orthogonal cutting with a temperature dependent friction law. J Mech Phys Solids 1998;46(10):2103–38.
[21] Komanduri R, Hou ZB. Thermal modeling of the metal cutting process - part II: temperature rise distribution due to frictional heat source at the tool-chip interface. International Journal of Mechanical Sciences 2001;43:57–88.
[22] Komanduri R, Hou ZB. Thermal modeling of the metal cutting process - part III: temperature rise distribution due to the combined e!ects of shear plane heat source and the tool-chip interface frictional heat source. International Journal of Mechanical Sciences 2001;43:89–107.
[23] Li L, Li B, Ehmann KF, Li X. A thermo-mechanical model of dry orthogonal cutting and its experimental validation through embedded micro-scale thin film thermocouple arrays in PCBN tooling. Int J Mach Tool Manuf 2013;70:70–87.
[24] Huang Y, Liang SY. Cutting temperature modeling based on non-uniform heat intensity and partition ratio. Machining Science and Technology 2006;9:301–23.
[25] M'Saoubi R, Chandrasekaran H. Experimental study and modelling of tool temperature distribution in orthogonal cutting of AISI 316L and AISI 3115 steels. The International Journal of Advanced Manufacturing Technology, journal article 2011;56(9):865–77.
[26] Karpat Y, Özel T. Predictive analytical and thermal modeling of orthogonal cutting process—part I: predictions of tool forces, stresses, and temperature distributions. J Manuf Sci Eng 2006;128:435–44.
[27] Karpat Y, Özel T. Predictive analytical and thermal modeling of orthogonal cutting process—part II: effect of tool flank wear on tool forces, stresses, and temperature distributions. J Manuf Sci Eng 2006;128:445–53.
[28] Shan C, Zhang X, Shen B, Zhang D. An improved analytical model of cutting temperature in orthogonal cutting of Ti6Al4V. Chin J Aeronaut 2019;32(3):759–69.
[29] Akbar F, Arsalan M. Thermal modelling of cutting tool temperatures and heat partition in orthogonal machining of high-strength alloy steel. Proceedings of the Institution of Mechanical Engineers, Part B: Journal of Engineering Manufacture 2021;235(8):1309–26.
[30] Zhou F, Wang X, Hu Y, Ling L. Modeling temperature of non-equidistant primary shear zone in metal cutting. International Journal of Thermal Sciences 2013;73:38–45.
[31] Avevor Y, Moufki A, Nouari M. Analysis of the frictional heat partition in sticking-sliding contact for dry machining: an analytical-numerical modelling. Procedia CIRP 2017;58:539–42.
[32] Veiga F, Arizmendi M, Jiménez A, Val AGD. Analytical thermal model of orthogonal cutting process for predicting the temperature of the cutting tool with temperature-dependent thermal conductivity. International Journal of Mechanical Sciences 2021;204:106524.
[33] Weng J, et al. Analytical and experimental investigations of rake face temperature considering temperature-dependent thermal properties. J Mater Process Technol 2023;314:117905.
[34] Barzegar Z, Ozlu E. Analytical prediction of cutting tool temperature distribution in orthogonal cutting including third deformation zone. Journal of Manufacturing Processes 2021;67:325–44.
[35] Hu C, Zhuang K, Weng J, Zhang X. Thermal-mechanical model for cutting with negative rake angle based on a modified slip-line field approach. International Journal of Mechanical Sciences 2019;164:105167.
[36] Liu H, Rodrigues L, Meurer M, Bergs T. A three-dimensional analytical model for transient tool temperature in cutting processes considering convection. CIRP Journal of Manufacturing Science and Technology 2023;43:1–14.
[37] M'Saoubi R, Chandrasekaran H. Experimental study and modelling of tool temperature distribution in orthogonal cutting of AISI 316L and AISI 3115 steels. The International Journal of Advanced Manufacturing Technology 2011;56:865–77.
[38] Marinov VR. Hybrid analytical numerical solution for the shear angle in orthogonal metal cutting - part I: theoretical foundation. International Journal of Mechanical Sciences 2001;43:399–414.
[39] Çelebi C, Özlü E, Budak E. Modeling and experimental investigation of edge hone and flank contact effects in metal cutting. Procedia CIRP 2013;8:194–9.
[40] Budak E, Ozlu E, Bakioglu H, Barzegar Z. Thermo-mechanical modeling of the third deformation zone in machining for prediction of cutting forces. CIRP Annals 2016;65(1):121–4.
[41] Saez-de-Buruaga M, Soler D, Aristimuño PX, Esnaola JA, Arrazola PJ. Determining tool/chip temperatures from thermography measurements in metal cutting. Appl Therm Eng 2018;145:305–14.
[42] Boothroyd G. Temperatures in orthogonal metal cutting. Proceedings of the Institution of Mechanical Engineers 1963;177(29):789–810.
[43] Merchant ME. Mechanics of the metal cutting process. I. Orthogonal cutting and a type 2 chip. J Appl Phys 1945;16(5):267–75.
[44] Rittel D, Zhang LH, Osovski S. The dependence of the Taylor–Quinney coefficient on the dynamic loading mode. J Mech Phys Solids 2017;107:96–114.
[45] Denkena B, Biermann D. Cutting edge geometries. CIRP Annals 2014;63(2):631–53.
[46] Wyen CF, Wegener K. Influence of cutting edge radius on cutting forces in machining titanium. CIRP Annals 2010;59(1):93–6.
[47] Zhou J, Ren J. Predicting cutting force with unequal division parallel-sided shear zone model for orthogonal cutting. The International Journal of Advanced Manufacturing Technology 2020;107:4201–11.
[48] Waldorf DJ, DeVor RE, Kapoor SG. An evaluation of ploughing models for orthogonal machining. J Manuf Sci Eng 1999;121(4):550–8.
[49] Ozlu E, Budak E, Molinari A. Analytical and experimental investigation of rake contact and friction behavior in metal cutting. International Journal of Machine Tools & Manufacture 2009;49:865–75.
[50] Childs TH, Maekawa K, Obikawa T, Yamane Y. Metal machining: Theory and applications. Butterworth-Heinemann; 2000.
[51] Shirakashi T, Usui E. Friction characteristics on tool face in metal machining. JSPE 1973;39(9):966–71.
[52] Malakizadi A, Hosseinkhani K, Mariano E, Ng E, Del Prete A, Nyborg L. Influence of friction models on FE simulation results of orthogonal cutting process. The International Journal of Advanced Manufacturing Technology 2017;88(9):3217–32.
[53] Shi B, Attia H. Modeling the thermal and tribological processes at the tool-chip interface in machining. Machining Science and Technology 2009;13(2):210–26.
[54] Hao G, Liu Z. The heat partition into cutting tool at tool-chip contact interface during cutting process: a review. The International Journal of Advanced Manufacturing Technology 2020;108:393–411.
[55] Matlab Documentation. Matlab, Massachusetts. 2020.
[56] Grzesik W. Advanced Machining Processes of Metallic Materials: Theory, Modelling and Applications. Elsevier; 2008.
[57] List G, Sutter G, Bouthiche A. 41 - List - cutting temperature predicition in high speed machining by numerical modelling of chip formation and its dependence on crater wear. International Journal of Machine Tools & Manufacture 2012;54-55:1–9.
[58] Shaw M, Cookson J. Metal cutting principles. New York: Oxford University Press; 2005.
[59] Malakizadi A, Cedergren S, Sadik I, Nyborg L. Inverse identification of flow stress in metal cutting process using response surface methodology. Simulation Modelling Practice and Theory 2016;60:40–53.
[60] Guo Z, Saunders N, Schillé JP, Miodownik AP. Material properties for process simulation. Mater Sci Eng A 2009;499(1):7–13.
[61] Lalwani DI, Mehta NK, Jain PK. Extension of Oxley's predictive machining theory for Johnson and Cook flow stress model. J Mater Process Technol 2009;209(12):5305–12.
[62] Fleischer J, Pabst R, Kelemen S. Heat flow simulation for dry machining of power train castings. Annals of the CIRP 2007;56:117–22.
[63] Olortegui-Yume JA, Kwon PY. Local crater wear prediction using physics-based models. J Manuf Sci Eng 2010;132(5).
[64] Fang N, Jawahir IS, Oxley PLB. A universal slip-line model with non-unique solutions for machining with curled chip formation and a restricted contact tool. International Journal of Mechanical Sciences 2001;43(2):557–80.
[65] Oxley LB, Hastings WF. Predicting the strain rate in the zone of intense shear in which the chip is formed in machining from the dynamic flow stress properties of the work material and the cutting conditions. Proceedings of the Royal Society of London: A 1977;356(1686):395–410.
[66] Fenton RG, Oxley PLB. Mechanics of orthogonal machining: allowing for the effects of strain rate and temperature on tool-chip friction. Proceedings of the Institution of Mechanical Engineers 1968;183(1):417–38.
[67] Jin X, Altintas Y. Slip-line field model of micro-cutting process with round tool edge effect. J Mater Process Technol 2011;211(3):339–55.
[68] Wang X, Jawahir IS. Recent advances in plasticity applications in metal machining: slip-line models for machining with rounded cutting edge restricted contact grooved tools. International Journal of Machining and Machinability of Materials 2007;2(3–4):347–60.
[69] Islam C, Altintas Y. A two-dimensional transient thermal model for coated cutting tools. J Manuf Sci Eng 2019;141(7).